Journal of Hydrometeorology

Increasing the depth of a Land Surface Model. Part I: Impacts on the subsurface thermal regime and energy storage

--Manuscript Draft--

Manuscript Number:	JHM-D-21-0024
Full Title:	Increasing the depth of a Land Surface Model. Part I: Impacts on the subsurface thermal regime and energy storage
Article Type:	Article
Corresponding Author:	Fidel Gonzalez-Rouco, Dr Universidad Complutense de Madrid Madrid, Madrid SPAIN
Corresponding Author's Institution:	Universidad Complutense de Madrid
First Author:	J. Fidel Gonzalez-Rouco, Dr
Order of Authors:	J. Fidel Gonzalez-Rouco, Dr
	Norman J. Steinert
	Elena García-Bustamante
	Stefan Hagemann
	Philipp de Vrese
	Johann H. Jungclaus
	Stephan J. Lorenz
	Camilo Melo-Aguilar
	Félix García-Pereira
	Jorge Navarro
Abstract:	The representation of the thermal and hydrological states in Land Surface Models is important for a realistic simulation of land-atmosphere coupling processes. The available evidence indicates that the simulation of subsurface thermodynamics in Earth System Models is inaccurate due to a zero-heat-flux bottom boundary condition being imposed too close to the surface. In order to assess the influence of soil model depth on the simulated terrestrial energy and subsurface thermal state, sensitivity experiments have been carried out in piControl, historical and RCP scenarios. A deeper bottom boundary condition placement has been introduced into the JSBACH land surface model by enlarging the vertical stratification from 5 to 12 layers, thereby expanding its depth from 9.83 to 1416.84m. The model takes several hundred years to reach an equilibrium state in stand-alone piControl simulations. A depth of 100 m is necessary, and 300 m recommendable, to handle the warming trends in historical and scenario simulations. Using a deep bottom boundary, warming of the soil column is reduced by 0.5 to 1.5 K in scenario simulations over most land areas, with the largest changes occurring in northern high latitudes, consistent with polar amplification. Energy storage is 3 to 5 times larger in the deep than in the shallow model and increases progressively with additional soil layers until the model depth reaches about 200 m. While the contents of Part I focus on the sensitivity of subsurface thermodynamics to enlarging the space for energy, Part II (Steinert et al. 2021) addresses the sensitivity to changing the space for water and improving hydrological and phase-change interactions.

Increasing the depth of a Land Surface Model. Part I: Impacts on the subsurface thermal regime and energy storage

J. F. González-Rouco* and N. J. Steinert

Department of Earth Physics and Astrophysics, Geosciences Institute IGEO (UCM-CSIC), University Complutense of Madrid, Madrid, Spain.

E. García-Bustamante

Research Centre for Energy, Environment and Technology (CIEMAT), Madrid, Spain.

S. Hagemann

Helmholtz-Zentrum Hereon, Geesthacht, Germany.

P. de Vrese, J. H. Jungclaus and S. J. Lorenz

Max Planck Institute for Meteorology, Hamburg, Germany.

C. Melo-Aguilar and F. García-Pereira

Department of Earth Physics and Astrophysics, Geosciences Institute IGEO (UCM-CSIC), University Complutense of Madrid, Madrid, Spain.

J. Navarro

Research Centre for Energy, Environment and Technology (CIEMAT), Madrid, Spain.

Corresponding author: J. F. González-Rouco, fidelgr@ucm.es

ABSTRACT

The representation of the thermal and hydrological states in Land Surface Models is important for a realistic simulation of land-atmosphere coupling processes. The available evidence indicates that the simulation of subsurface thermodynamics in Earth System Models is inaccurate due to a zero-heat-flux bottom boundary condition being imposed too close to the surface. In order to assess the influence of soil model depth on the simulated terrestrial energy and subsurface thermal state, sensitivity experiments have been carried out in piControl, historical and RCP scenarios. A deeper bottom boundary condition placement has been introduced into the JSBACH land surface model by enlarging the vertical stratification from 5 to 12 layers, thereby expanding its depth from 9.83 to 1416.84 m. The model takes several hundred years to reach an equilibrium state in stand-alone piControl simulations. A depth of 100 m is necessary, and 300 m recommendable, to handle the warming trends in historical and scenario simulations. Using a deep bottom boundary, warming of the soil column is reduced by 0.5 to 1.5 K in scenario simulations over most land areas, with the largest changes occurring in northern high latitudes, consistent with polar amplification. Energy storage is 3 to 5 times larger in the deep than in the shallow model and increases progressively with additional soil layers until the model depth reaches about 200 m.While the contents of Part I focus on the sensitivity of subsurface thermodynamics to enlarging the space for energy, Part II (Steinert et al. 2021) addresses the sensitivity to changing the space for water and improving hydrological and phase-change interactions.

1. Introduction

Earth System Models (ESMs) are at the highest level in the hierarchy of complexity of coupled general circulation models (GCMs; McGuffie and Henderson-Sellers 2005). They have evolved to realistically represent many of the processes that generate climate variability and can be used to analyze sensitivity to changes in or the interactions between climate subsystems, ultimately being the key tool to assess climate change (Pachauri and Mayer 2014; Knutti et al. 2017; Masson-Delmotte et al. 2018). The complexity of ESMs has increased with the inclusion of a progressively larger number of GCM components and processes and with an increasing level of realism in representing them. Modeling of radiation, aerosol-cloud interactions, cryosphere, biogeochemical cycles and other features has been improved or newly included through the most recent phases of the Coupled- and Paleo- Model Intercomparison Project (CMIPs, PMIPs; Taylor et al. 2012; Cubasch et al. 2013; Eyring et al. 2016; Simpkins 2017).

In spite of their complexity and model performance showing a high level of realism (e.g. Flato et al. 2013), ESMs can only be a reductionist version of reality (Oreskes et al. 1994). The representation of elements, mechanisms and interactions in the system involves diverse levels of simplification, including the possibility of being excluded because of being considered irrelevant, computationally unaffordable or just being unknown and ignored (von Storch 2010; Palmer and Stevens 2019). One of such examples for simplification can be found in the context of modeling of subsurface thermodynamics in Land Surface Models (LSMs).

LSMs have experienced significant progress in the last generations of ESMs (Cubasch et al. 2013), including new and more realistic biogeophysical and biogeochemical processes (Lawrence et al. 2011, 2012; Bonan and Doney 2018), thereby considering carbon and nitrogen cycles, river routing, vegetation dynamics, transient land use and land cover (LULC) changes, characterization

of the snow pack layering and other processes (e.g. Bonan et al. 2018; de Vrese et al. 2018; Krinner et al. 2018; Lawrence et al. 2019; Mauritsen et al. 2019; Hagemann et al. 2020). Subsurface thermodynamics have also experienced progress in the simulation of water phase changes, dynamic heat capacity and conductivity parameterizations, interactions with hydrology as well as influences on permafrost dynamics and carbon and nitrogen pools (e.g. Ekici et al. 2014; Hagemann et al. 2016; McGuire et al. 2018).

Below the surface, temperatures are determined by changes at the surface (e.g. Melo-Aguilar et al. 2018) and by the conductivity and capacity of different organic and mineral soil types and the concentration of water that modulates their effective values (Pollack et al. 2005) down to the bedrock level, beyond which rock properties are homogeneous with depth. In the absence of advection and convection, the thermal regime is conductive and temperature changes at the surface propagate downwards depending on the effective diffusivity (Carslaw and Jaeger 1959; Turcotte and Schubert 2002). However, modeling of subsurface heat transport has barely changed in ESMs during the last decades.

Conductive diffusion dampens and lags surface temperature changes propagating with depth. The details of this propagation in LSMs and their hosting ESMs depend on the vertical discretization, that includes in all LSMs/ESMs a zero-energy-flux condition at the bottom layer, thus ensuring energy preservation in the ESM. Model depth and the characteristics of the heat diffusion regime are determined by this bottom boundary condition placement (BBCP hereafter).

A realistic simulation of subsurface thermodynamics and downward heat transport is an important aspect in LSMs within ESMs, with implications for the surface energy balance, energy transport and storage under the Earth's surface as well as for soil hydrology (Koster et al. 2006; Guo et al. 2006; Seneviratne et al. 2010; Melo-Aguilar et al. 2018). Ideally, such modeling should involve downward propagating temperature changes that are not limited by a zero-flux condition at any

depth during the time span of the simulation. This is tantamount to the BBCP being detached from the surface, i.e. to defining an infinite half space below the surface (Turcotte and Schubert 2002).

Downward heat transport is frequency dependent and longer (shorter) period waves attenuate less (more) with depth. For instance, the annual cycle is hardly perceptible at 20 m and two centuries of climate change warming would propagate down to a depth of about $200-250\,m$ (Mareschal and Beltrami 1992; Pollack and Huang 2000). Therefore, the depth of the LSM should also be adapted to accommodate the long-term trends in the simulated period (Smerdon and Stieglitz 2006; Alexeev et al. 2007). However, the current generation of ESMs have BBCPs that range between 2 and 10 m (Cuesta-Valero et al. 2016), with the exception of the Community Land Model (e.g. Oleson et al. 2010; Lawrence et al. 2019) in the Community Earth System Model (e.g Otto-Bliesner et al. 2016; Melo-Aguilar et al. 2018) where the BBCP is $33.74m$ deep, at the bottom layer with a lower limit of 43.74 m. Even the latter is, *a priori*, an insufficient depth to accommodate bi-century long-term trends of historical and scenario experiments into the subsurface.

Heat transport in the Earth's subsurface plays an important role in governing water, energy and momentum fluxes at and below the surface. Their simulation can be affected by shallow BBCPs distorting the behaviour of the downward propagating temperature signals in comparison to the realistic infinite half space by slowing the rate of their amplitude damping and enhancing phase shift with depth. This has been demonstrated analytically (Smerdon and Stieglitz 2006), in LSM exercises (Lynch-Stieglitz 1994; Sun and Zhang 2004; Alexeev et al. 2007) and shown for interannual and multi-decadal timescales in GCM simulations with a shallow BBCP (González-Rouco et al. 2009). Shallow models result in too sensitive soil temperatures near the surface that significantly overestimate variability at all timescales (Alexeev et al. 2007).

CMIP5 historical and scenario experiments simulate a progressive soil warming during the 20th century, slightly slower than that of air warming and their difference increases over the 21st century

(Soong et al. 2020). Simulated regional soil and air warming rates are similar in tropical and arid regions while the soil lags the air warming at high-latitudes due to the combined influence of external forcings (e.g. greenhouse gas, aerosol and LULC) and snow feedbacks (Melo-Aguilar et al. 2018). High-latitude soils are projected to warm faster than elsewhere albeit at slower rates than the air temperatures above (Soong et al. 2020; Melo-Aguilar et al. 2018). Soil temperature projections are important for ecosystem, food production and carbon budgets (Huang 2016; Zhao et al. 2017; Wu et al. 2018) and the confinement of energy in current shallow LSMs can lead to overstating heat storage and temperature variability in the first few meters of the ground. However, the impacts of including realistically deep BBCPs in ESMs have not yet been considered (Phillips 2020).

Additional to the simulation of the thermal state, deeper BBCPs offer larger storage space for energy. It is virtually certain that the Earth has gained energy in the last four decades with a permanent energy imbalance at the top of the atmosphere (Trenberth et al. 2009; Hansen et al. 2005, 2011). The evaluation of energy inventories by Rhein et al. (2013) partitioned the relative energy storage in the Earth system into ocean warming (93 %), cryosphere melting (3 %), and litosphere (3 %) and atmosphere (1 %) warming; the numbers for the ocean, cryosphere and litosphere being recently revised with a higher contribution of the land subsurface to 89 %, 4 % and 6 %, respectively (Cuesta-Valero et al. 2020; von Schuckmann et al. 2020). Therefore, even if the ocean has the dominant contribution to the Earth's energy storage (Levitus et al. 2012; Ortega et al. 2013), there is a role of the land component in the global energy balance. However, CMIP5 models show lower magnitude of continental energy storage than observational estimates from geothermal data with inter-model variability, relating to differences in BBCPs to a large extent (Cuesta-Valero et al. 2016). This is supported by studies based on the comparison of borehole records and last millennium climate simulations. For instance, analysis of shallow BBCP

climate model energy storage since pre-industrial times (González-Rouco et al. 2006) and that from borehole records (Beltrami et al. 2006) renders an underestimation of energy by the climate model that is only corrected when offline LSMs are used with realistic BBCPs to account for the extra energy storage (Stevens et al. 2007; MacDougall et al. 2010). Differences of land energy storage in climate change experiments with offline LSMs have been found to be larger between deep and shallow BBCPs than for different scenarios (MacDougall et al. 2008; González-Rouco et al. 2009). A recent evaluation expanding the depth of the Community Land Model (CLM4.5; Oleson et al. 2013) from 42.1 m to 342.1 m with simulations spanning the period 1900 to 2300 AD by Hermoso de Mendoza et al. (2020) shows that heat storage increases by a factor between 1.7 to 3.6 depending on the length of the simulation considered. Consequently, an evaluation of the importance of a realistic estimate of the subsurface thermal state and energy storage for ESMs are still pending and arguably relevant in simulations during which the land systematically gains or loses energy during long time intervals, as in the case of historical and climate change scenario experiments (Phillips 2020).

This work addresses the impact of lowering the BBCP on soil thermodynamics and heat storage in stand-alone historical and scenario simulations of JSBACH (Hagemann et al. 2013), which is the land surface component of the Max-Planck-Institute for Meterology ESM (MPI-ESM hereafter; Mauritsen et al. 2019). The LSM is forced off-line with data from fully coupled simulations of the MPI-ESM for the historical period and climate change scenarios. The LSM and ESM correspond to the current version used for CMIP6 experiments. We analyze the stepwise changes in soil temperatures and energy storage when the model is progressively expanded from a BBCP-depth of 9.83 m using 5 model layers, to a depth of 1416.84 m with 12 model layers. We consider the time of convergence to equilibrium needed by the LSM as its depth is increased as a relevant matter for subsequent land-atmosphere and fully coupled ESM experiments. We analyze the impacts on

the soil conduction regime and the resulting distribution of temperature changes as well as energy storage.

Furthermore, lowering the depth of the BBCP does not only impact the thermodynamics, but is also relevant for thermal and hydrological interactions. Since the energy and hydrological cycles are closely related, considering different datasets to those prescribed and/or physics options that are not standard in the CMIP6 version of the model allows for assessing the sensitivity to water phase changes in permafrost areas, snow layering, dynamic conductivity and heat capacity modeling (Lawrence et al. 2008; Hagemann et al. 2016; Ekici et al. 2014; Heidkamp et al. 2018). All these options can change the spatial distribution of subsurface water and thermodynamics and ultimately the space available for energy storage. Such sensitivity changes are addressed in the context of a realistic BBCP in a companion paper (PartII, Steinert et al. 2021).

2. Model description and experiment setup

The MPI-ESM1.2 version (Mauritsen et al. 2019) modeling frame is used herein. This is the reference version for the CMIP6 (Eyring et al. 2016) experiments and it has undergone several developments since the MPI-ESM version used for CMIP5 (Giorgetta et al. 2013). MPI-ESM consists of four model components that are integrated into the atmosphere and ocean model blocks, both communicating through the OASIS3-MCT coupler (Craig et al. 2017). The ocean model is MPIOM1.6 and includes a tracer advection biogeochemistry model (HAMOCC6; Jungclaus et al. 2013; Ilyina et al. 2013). The atmosphere model (Stevens et al. 2013; Roeckner et al. 2003) version is ECHAM6.3, which is directly coupled to the LSM version JSBACH3.2 (JSBACH hereafter; Raddatz et al. 2007; Brovkin et al. 2009; Hagemann et al. 2013) through surface exchange of mass, momentum, and heat.

The individual model components can also be operated in stand-alone mode. Herein, the JSBACH model has been run in stand-alone mode with boundary conditions provided from piControl, historical and scenario simulations from CMIP5 ECHAM6 in fully coupled MPI-ESM experiments (Stevens et al. 2013).

a. Land Surface Model

JSBACH is a comprehensive terrestrial ecosystem model with a process-based approach for representing key ecosystem functions: photosynthesis, phenology and land physics with hydrological and biogeochemical cycles (Raddatz et al. 2007; Brovkin et al. 2009). JSBACH version 3.20p1 is used herein; see Hagemann et al. (2016) for improvements since the JSBACH 2.0 version used in CMIP5.

Figure 1 provides a scheme for the different elements that are considered at the land surface and below, and are relevant for this work; see also the complementary discussion in Steinert et al. (2021). The horizontal resolution of JSBACH is set to T63, which corresponds to roughly 1.85 degrees on a homogeneous grid, consistent with that of the atmospheric GCM. Land surface albedo is calculated separately for the visible and near infrared, and includes a consideration of the bare surface fraction, snow on soil, and canopy effects, including forest masking (Brovkin et al. 2013; Nabel et al. 2020). Grid cells are assigned tiles of homogeneous vegetation cover including 12 plant functional types and two types of bare soil surface; dynamic vegetation is optional. A detailed technical description of the land cover parameterization is given in Reick et al. (2013). The soil carbon model (Goll et al. 2015) is not activated and vegetation cover is herein prescribed and kept constant over time. This is the case for both Part I herein and Part II Steinert et al. (2021).

To simulate the land surface and soil processes in JSBACH, heat and water diffuse vertically and no horizontal diffusion is allowed. The energy and water exchange within the soil is described

by a multi-layer vertical grid that grows in thickness with increasing soil depth (Fig. 1). Surface temperature is calculated by considering incoming radiation and surface albedo. In the presence of snow, the top of the snow layer is considered as the top of the soil model (Schulz et al. 2001) and the bottom snow layer is used to force the soil column. The snow pack is represented up to two layers that thermally grow down inside the soil (Fig. 1); i.e. the snow cover becomes part of the soil temperature layers so that soil temperatures are mixed with snow temperatures. For snow covered land, a mass-weighted mixture of soil and snow is applied to determine the thermal properties, i.e., if the snow fills the top soil layer completely, and the next one partially, the respective properties for snow are used for the top layer and a mass-weighted mixture is used for the next one. The impacts on subsurface thermodynamics of considering a more realistic layering of the snow pack by increasing discretization and placing it above the surface as in Ekici et al. (2014) are evaluated in Steinert et al. (2021).

Rainfall and snowmelt are distributed into surface runoff, infiltration and lateral drainage (Dümenil and Todini 1992). The vertical transport of water takes place through diffusion and percolation (e.g. van Genuchten 1980) in a five-layer scheme (Hagemann and Stacke 2015) that replaced the previous single-layer bucket model in Stevens et al. (2013). The five layers with increasing thickness are defined with a lower boundary at 9.83 m that corresponds directly with the structure used for soil temperatures (Fig. 1). The space for water storage is limited to the soil above the bedrock, while the plant available water is limited to the root zone. The number of moisture-active layers is thus limited by the depth down to the bedrock. There is no moisture below that level. Water can drain when the soil reaches a minimum level of saturation and within the root zone the water can also be taken up by plants and be transpired. The water stored on land is a key variable controlling numerous processes and feedbacks on the water and energy cycles. Thus, changes in the thermodynamics can potentially derive from changing the space for water by considering different

datasets involving uncertainty in the estimations of root and bedrock depths. The sensitivity to these changes is also explored in Steinert et al. (2021).

Conduction is the only method of heat transport considered since the contribution from geothermal radioactive decay is small and convective and advective heat transport is related to fluid motion and disregarded (Carslaw and Jaeger 1959; Turcotte and Schubert 2002). The subsurface vertical temperature profile is calculated by following the one dimensional heat diffusion equation (Carslaw and Jaeger 1959). The original Warrilow et al. (1986) scheme in an early release of the European Center (EC) Medium Range Weather Forecasts climate model was expanded to 5 layers (Fig. 1, Table 1) in the design of the first MPI Hamburg (HAM) atmospheric GCM (ECHAM Roeckner et al. 1989, 1992). A zero-flux BBCP was ensuring energy preservation at the lowest layer having a center at 6.98 m and reaching 9.83 m at its lower limit.

This vertical discretization is expanded herein progressively to 12 layers with depths and thickness shown in Table 1, reaching a BBCP at the bottom layer with a center at 1068.24 m and a lower limit at 1416.84 m. The expansion is done by best fitting an exponential function to the existing thickness configuration of 5 layers and using it to estimate the values of the thickness for the 7 layers below so that the progression of layer growth is consistent with the currently existing one. The form of the function follows Oleson et al. (2010) and is used to obtain thickness with $th(i) = a_1 \exp\left[a_2(i - a_2) + a_3\right]$, with i being the layer number and a_j, with $j = 1\ to\ 3$, the coefficients resulting from the fit. The $th(i)$, $i = 1\ to\ 5$, were used to estimate the a_j, obtaining values $a_1 = 0.33 \pm 0.16$, $a_2 = 0.6738 \pm 0.12$, $a_3 = -1.45 \pm 0.46$ ($p < 0.05$). These a_j were used to estimate the thickness of layers 6 to 12 in Table 1.

Thermal properties, such as the volumetric heat capacity and thermal conductivity for different soil types are obtained from the Food and Agriculture Organization of the United Nations (Dunne and Willmott 1996) soil map. In the version of the model used herein they are defined constant for

the whole soil and bedrock column; thus, the bedrock is considered only to limit hydrology. Also, soil heat transfer is not coupled to the hydrological scheme. For more details about soil parameters and global bedrock data, see Hagemann and Stacke (2015). In a variant model version, energy and hydrology are coupled through latent heat from water phase changes and the thermal parameters, volumetric heat capacity and soil heat conductivity that change dynamically depending on the water content (Ekici et al. 2014). The sensitivity to using these variant options is explored in the companion paper (Steinert et al. 2021).

Changes in the surface energy and water balance are applied to the LSM in stand-alone mode by prescribing surface boundary conditions. Temperature and water changes diffuse downwards through the soil, down to the bedrock level (Fig. 1). Energy continues being transported below the bedrock down to the maximum depth of the BBCP. According to Pollack and Huang (2000), for a signal lasting the 250 years of post 1850 CE historical and scenario climate change experiments up to 2100, a depth of about 300 m should be sufficient to accommodate the downward propagating temperature perturbation into the ground. Thus, the last two or three layers in Table 1 allow the LSM for having a detached BBCP from the surface and for the possibility of accommodating even multi-centennial long experiments in future studies.

b. Experimental setup

The assessment is focused on analyzing the impact of increasing LSM depth on historical and climate change experiments. The experiment design follows the scheme in Figure 2. JSBACH is run first in 8 piControl (PIC) experiments that allow for a stepwise increase of the BBCP beyond layer 5 (5L in Fig. 2) to layer 12 (12L). The PIC experiments simulate a continuous climate state compatible with the 1850 external forcing and provide initial conditions for the historical runs (HIS; 1850 to 2005), that are subsequently continued in climate change Representative Concentration

Pathway (RCP) experiments for the 2006 – 2100 period, specifically RCP2.6, RCP4.5 and RCP8.5. These experiments are driven by boundary conditions provided by data from fully coupled MPI-ESM simulations that comply with piControl, historical and RCP forcing specifications of CMIP5 (Taylor et al. 2012; Stevens et al. 2013). The RCP6.0 scenario is not included, since no atmospheric forcing files for the standalone JSBACH exist from the CMIP5 MPI-ESM (e.g. Giorgetta et al. 2013). An evaluation of the combined land-surface energy and water fluxes in the frame of the MPI-ESM for CMIP5 is given in Hagemann et al. (2013).

In the case of the PIC experiments, each simulation is started from the same arbitrary initial state and continued for 500 years. The initial state of the different 5L to 12L experiment variants is identical for the layers they share so that, for instance, the 12L experiment variant has identical initial conditions to the 11L experiment for its 11 upper layers. Since the PIC simulations can be as long as needed, depending on the purpose, this would require having boundary conditions available for any given length of a piControl simulation. In order to avoid this dependence, boundary conditions are provided only for a segment of MPI-ESM data that are continuously concatenated to drive the JSBACH model. This allows for running the LSM as long as it is needed with a small amount of prescribed data and focus on the long-term response of the model. The length of this forcing data is 28 years. As a result, the simulated temperature variability will show an artificial 28 year timescale that is phase locked to this period of 28 years in the boundary conditions. This cycle can be filtered out to analyze long-term trends in the PIC runs. The length of the experiments has been accommodated to allow for the deepest LSM variants to reach equilibrium.

c. Convergence to equilibrium

Figure 3 shows the evolution of global (top) and Northern Hemisphere (NH) latitudes (bottom) soil temperatures for the 12L PIC experiment. The 28 year timescale induced by the boundary

conditions is visible and can be well identified in the shaded area that highlights the last cycle of 28 years. The attenuation of variability and phase shift of temperature changes with depth resulting from heat diffusion is visible in both panels.

The attenuation of temperature variability can be illustrated by the amplitude damping in the top five layers for frequencies below the annual cycle by using spectral analysis. The amplitude of each harmonic component at the first and fifth layer can be obtained using a spectral analysis for which ordinates have been transformed to represent the amplitude of the wave at each frequency as in González-Rouco et al. (2009). The ratio of spectral amplitudes for the time series at the first and fifth level provides an estimation of the amplitude damping at each frequency. Figure 4 shows this analysis for an arbitrary grid-point at the Sahara, selected in the deep (12L) and shallow (5L) models (solid lines in black and red, respectively). The expected ratio of amplitude spectra is also shown for the resulting curves from the analytical solutions of the conductive regime in the shallow case and in an infinite half space (dashed lines) following Smerdon and Stieglitz (2006). The amplitude attenuation is in good agreement with the changes expected from the analytical solutions of both conductive regimes, highlighting that in the shallow model the variability near the surface is damped considerably less than in the deep model version. It also shows that the 12L model behaves realistically as an infinite half space.

Average temperatures in Figure 3 are slightly larger for the first level globally and particularly at northern latitudes resulting from snow cover insulation and melting effects (Melo-Aguilar et al. 2018). For northern high latitudes there is an initial offset of about 1.5 K between the top and bottom soil layers. At global scales, temperatures are stable throughout the simulation but at northern high latitudes, they show long-term adjustments towards equilibrium. Convergence to equilibrium takes place at different timescales for the various model layer depths as expected from heat diffusion. The drift is larger for intermediate layers and lasts over centuries. The drift does

not seem to happen for the last two layers centered at 542.06 m and 1068.24 m, thus indicating detachment from surface changes.

For a better description of the long-term trends in PIC soil temperatures, Figure 5 shows differences for all model levels with respect to the years 473 to 500 of the simulation (shaded area in Fig. 3). The values of the last 28-year interval (shaded area in Fig. 3) are subtracted from those of each 28-year segment established by the repeated boundary conditions, thus filtering out the synthetic timescale in the resulting anomalies. The dashed lines represent two sigma deviations from the mean in the resulting anomalies for the 500 years of simulation. Convergence to equilibrium needs about 200 years for global soil temperature averages, as discussed in Figure 3, although most of the temperature change is accommodated in the first 50 years. The temperature change is relatively small and only of a few hundredths of a degree. If latitudinal bands are considered, a variety of drift responses is found with: the extratropical latitudes showing temperature changes of about two tenths of a degree warming (cooling) in the Southern Hemisphere (Northern Hemisphere); intertropical latitudes and higher latitudes of the Southern Hemisphere (SH) showing warming drifts of half a degree; and the largest changes taking place at high latitudes (60°N–90°N) of the NH where changes can be about 1.5 K for some layers. At all latitudinal bands, the largest changes are for the top soil layers and the timescale of convergence increases progressively with depth down to layer 9. Changes for layer 10 are minor and unnoticeable for layers 11 and 12, thus confirming their detachment from the surface. After 400 years, the rate of adjustment for layer 9 is very slow and of *ca.* $-0.1\ K/century$ for the 60°N–90°N region, which can at the most introduce a comparably small bias of this magnitude in the subsequent simulations for the HIS and RCP forcing scenarios.

Therefore, these results show that even in a PIC simulation, which does not include long-term changes in forcing, the 5-layer model with a BBCP-depth of 9.83 m is too shallow and compromised

in representing soil thermal activity. The surface temperature variability propagates to at least a depth of 138 m, the 9th layer considering the vertical discretization used herein.

The depth and number of layers that are thermally active will depend on the vertical discretization adopted. Note that since the PIC simulations do not involve responses to long-term trends in forcing, Figures 3 and 5 are only illustrative of the adjustment needed for the initial conditions. These adjustments may also vary depending on the design of the initial state and how much it departs from equilibrium, not only at global but also at regional scales. This may be of relevance for establishing initialization strategies in LSMs coupled to an atmospheric GCM and in fully coupled ESM simulations since the computing resources required by them are much larger. Note that even the same model can have different states of equilibrium depending on the model setup or coupling strategies to other climate subsystems.

d. External forcing influences on the soil temperature response

The transient 12L simulation (Fig. 6a) shows that the surface warming has a strong influence on the first model layer at 0.06 m, with a temperature increase of about 6 K in the last 30-year average of the RCP8.5 simulation with respect to the PIC level. This number is in the range of those given by Soong et al. (2020) for current CMIP5 simulated soil temperatures. The long-term increase in surface temperature is almost 1.5 K until the beginning of the RCP simulations and rises to about 4 K until the last 30 years of the RCP8.5 simulation, during which a total increase of 6.5 K relative to pre-industrial is attained. The temperature response is most noticeable in the HIS simulation after the 1970s and propagates down to the 8th level reaching a depth of 91.73 m and affecting only minimally the 9th model level sitting at 183.66 m. The amplitude of the high-frequency fluctuations decreases with depth as well as the amplitude of the long-term warming trends. The right panel in Figure 6a shows the range of the response for the last 30 years of the 21st century

in the three simulated scenarios and all levels. RCP4.5 (RCP2.6) shows soil temperature increases of almost 3 K (2 K) relative to the pre-industrial state. The range of the temperature increase in the last three decades of the 21st century is depicted by the width of the box and whiskers plots and diminishes with the lower warming in the less intense scenarios. At each scenario, the range of warming is comparable for the four top layers, as shown in Soong et al. (2020), and diminishes progressively to the 8th layer, where a warming of 0.2 K, relative to PIC, is found for any of the three RCPs. The temperature increase is negligible for layer 9 and the last three layers, showing that the BBCP is virtually detached from the temperature changes at the surface.

The question that arises is how the thermal state of the soil changes because of having a deeper BBCP that allocates more space for energy distribution into the soil and that can alter the propagation of temperature perturbations with depth (Smerdon and Stieglitz 2006) and thus, the conductive regime. If the simulated 12L deep LSM configuration is compared with the 5L shallow one, some insights into the influence of deepening the BBCP can be gained. Differences in the soil temperatures of the five top layers in the 12 LSM simulation with respect to the 5 layers of the 5L simulation show a relative cooling (Fig. 6b) that starts at the time of the warming trends in the 1970s and progressively increases towards the end of the simulation. The effect of the difference in the attenuation of the temperature amplitude and the phase shift between the two model configurations is not evident near the surface due to the influence of the boundary conditions on the upper model layers. Since the conduction of temperature changes takes place on very short timescales at that depth and there is a strong lead of the boundary conditions, this prevents feedbacks from subsurface temperatures propagating closer to the surface. Below the second level, differences become noticeable and the 12L LSM becomes cooler than the 5L model, with the differences being larger for layers 4 and 5, where changes of about 0.3 and 0.8 K, respectively, are attained by the end of the RCP8.5 simulation. For the weaker RCP4.5 and

RCP2.6 scenarios, the relative cooling in layers 4 and 5 is of the order of 0.3 K (RCP4.5) and 0.15 K (RCP2.6).

The largest differences in Figure 6b are attained for the 5th model level. Figure 6c-f shows the spatial distribution of temperature differences for this level between the deep 12L and shallow 5L model cofiguration in the last 30 years of the three transient simulations. Changes are of a few tenths of a degree and widespread for the historical and RCP2.6 and RCP4.5 scenarios. Some partly glaciated regions like the Himalayas and the Andes show slight relative warming in HIS and RCP2.6 due to differences in ice diffusivity (Melo-Aguilar et al. 2018). In the RCP8.5 scenario, differences of 1 K are widespread and in the NH high latitudes they can exceed 1K.

It is also interesting to see the occurrence of sudden cooling in soil temperatures in Figure 6a,b due to volcanic activity like the Krakatoa (1883) and the Pinatubo (1991; Gao et al. 2008; Crowley and Lowery 2000), which produces a relative warming in the deep LSM in comparison to the shallow one. This illustrates that the deep soil acts as a buffer damping the changes in the upper meters of the soil-column (Smerdon and Stieglitz 2006; Alexeev et al. 2007). This can be better seen in Figure 7 that shows a Hovmöller representation of temperatures *vs.* depth in the 5L and the 12L LSM configurations for the last century in the PIC simulations, continued in the HIS and through the RCP8.5 scenario. Note that the depth scale is logarithmic and the line at 9.83 m in Figure 7d represents the bottom boundary of the 5th layer and the beginning of the downward expansion of the BBCP in the deep model version. The progression of the warming with depth is evident in both configurations. However, for the 5L configurations, the warming is spread immediately over the full depth of the model, whereas in the 12L LSM version, warming propagates progressively through the first dozens of meters reaching 100 m, well over layer 8, by 2050; recall that 10 m is less than the distance travelled by the annual cycle (Pollack and Huang 2000).

The damping of the warming, i.e. the relative cooling effect of the deep BBCP model version in the top five layers, is also evident if the lower part of the first 10 m are compared in both model variants. Figure 7g represents the differences between both configurations for the 5 top model layers. The relative cooling starts in the 1970s with the beginning of the warming trends and progresses upwards during the 21st century to the values reported in Figure 6. During the end of the PIC and the HIS intervals, differences show a succession of weak positive and negative intervals that correspond with cooling and warming intervals in the simulations, thus indicating that even in the absence of long-term trends, the influence of the deep BBCP configuration is to counterbalance the sign of the surface temperature changes. This succession of alternating positive and negative differences progressively weakens in the first half of the 20th century and gives way to negative values when the long-term warming trends start during the second half of the 21st century.

Temperature anomalies at the end of the RCP scenarios are shown in Figure 7c,f for the 5L and 12L configurations relative to the state of soil temperatures at the first model level by the end of the PIC simulation. The results are similar to each respective layer since all layers start from a very similar state globally (Fig. 6a). The changes in the thermal state are very homogeneous for the 5 layers in the shallow configuration and depict warmings of 6 (RCP8.5), 3.5 (RCP4.5) and 2.5 (RCP2.6) K for the 10 m bellow the surface (Fig. 7c). The deep BBCP dampens the warming visibly in the last three layers with differences that reach 0.8 K in RCP8.5, 0.35 K in RCP4.5 and 0.15 K in RCP2.6 (Fig. 7c,i). Figures 7b,e,h show the diversity of responses in RCP8.5 for several latitudinal bands indicating that the largest warming in the last years of the century ($\sim$ 9 K) occurs for NH high latitudes (blue), followed by intertropical and NH mid latitudes ($\sim$ 6 K).

Overall, the spatial distribution of changes induced by deepening the BBCP is very homogeneous, both geografically and within the first 10 m of the ground as shown in Figures 6 and 7, with the largest impact impinging on northern high latitudes. Figure 8 expands the information provided

by Figure 6 for different latitudinal bands as an example. Note that in Figure 8, the absolute scales are different but they cover the same temperature range. The high and mid latitudes of the SH show the lowest warmings of about 5 K for the top soil layer at the end of the RCP8.5 simulation (not shown); on average 4 K for the last three decades of the 21st century. The largest changes are attained in the high latitudes of the NH, where warming of about 10 K (8 K on average for the last three decades) is reached (Fig. 8). Due to snow cover effects at these latitudes (Melo-Aguilar et al. 2018) temperatures are slightly lower in the first layer than for the two layers below during all the simulation and stay lower at the end of the 21st century. The temperature increase reaches the 8th layer with a rise of 1 K or more for all latitudinal bands and is negligible for the 9th layer. Thus, for all regions the BBCP is detached from surface changes. Also, at all latitudinal bands, the subsurface is colder than the simulation with the shallow model (Fig. 8). The relative cooling is largest for the 5th and 4th layers and it ranges from 0.5 K and 0.2 K, respectively, in the SH high and mid latitudes to 1.25 K and 0.5 K, respectively, in the NH high latitudes. At these latitudes the cooling effect is even noticeable for layer 2 within the first meter of the ground. Therefore, keeping the shallow model configuration contributes to increase the temperature of the simulated subsurface relative to the realistic situation with a detached BBCP. Additionally, within the historical and scenario simulations, using a detached BBCP has an impact at depths below those of the usual BBCP position in the MPI-ESM.

Figure 9 (top) synthesizes the results for the three scenarios and the number of model layers used. For all scenarios, results tend to group into three levels of response. High latitudes of the NH show the largest temperature change at the end of the 21st century with increases of 9K (RCP8.5), 5 K (RCP4.5) and 3.5 K (RCP2.6), showing notably less warming for the 5th bottom layer in RCP8.5 (> 1 K) and RCP4.5 (0.5 K) and for the 4th layer in RCP8.5 (0.4 K). The smallest temperature changes can be found in the SH mid and high latitudes with temperature increases of about 4.7 K

(RCP8.5), 2.5 K (RCP4.5) and 1.5 K (RCP2.6), The temperature rise is less pronounced for the detached BBCP in the 5th layer in RCP8.5 (> 0.5 K) and RCP4.5 (0.3 K) and for the 4th layer in RCP8.5 (0.2 K). The remaining latitudinal bands and the global case show intermediate responses for which again layers 4 and 5 show the largest warming attenuation with the deeper BBCP, mostly in the two strongest RCP scenarios. Note that in all cases the shallow model configuration tends to show a very homogeneous response through all layers that align vertically in the diagram, whereas the deep BBCP tends to spread the response downwards producing less warming, i.e. relative cooling, in the layers above the shallow BBCP. It would remain to assess whether the spread would propagate also to the top layers in a case in which the atmospheric GCM and the LSM would be coupled instead of the present case in which the LSM is driven stand-alone with no possibility of interaction.

The inclusion of the deeper BBCP acts progressively to damp the warming as additional soil layers are added. This can be seen in the 5th layer soil temperature differences between the configurations in which a new layer is added stepwise with respect to the same layer in the 5L reference configuration (Fig. 9, bottom). For all scenarios adding the 6th soil layer shows an increased relative cooling that is larger for the NH and becomes larger when the 7th and 8th layers are added stepwise. This happens for all RCPs and latitudinal bands, although with different levels of response. The inclusion of layers 9 to 12 produces slight and, for most cases, unnoticeable changes.

Figures 7 to 9 demonstrate the relative cooling in the upper subsurface in the deep model relative to the shallow LSM. This is an indication that the warming of layers 6 to 9 is the result of heat transport and accumulation of energy in the added layers instead of energy staying locked above the shallow BBCP of the 5L LSM.

e. Energy storage

The changes in the energy balance in the Earth System due to changes in external forcings are here introduced in the LSM through changes in surface boundary conditions. A part of the incoming energy, which increases with the rise in external forcing, will be stored into the subsurface. In the case of HIS, in a shallow BBCP configuration, global mean annual terrestrial heat content change (AHCC) is in the range of $0-5\cdot10^5 Jm^{-2}yr^{-1}$ (Fig. 10). Similar energy storage takes place in RCP4.5 and RCP2.6, whereas in RCP8.5 the amount of energy stored increases by a factor of two ($5-10\cdot10^5 Jm^{-2}yr^{-1}$; Fig. 10). For comparison, recall that recent estimates of Earth System rates are on the range of $132.5\cdot10^5 Jm^{-2}yr^{-1}$ (von Schuckmann et al. 2020).

In general, introducing a deeper BBCP amplifies the range of energy loss/gain in various regions in comparison to the shallow model in HIS (Fig. 10, right). While in general there is widespread warming and an increase of energy storage, a regionally more complex pattern arises. Indeed, some areas where the surface temperature trends are negative during some decades of the HIS period and do not show energy storage in the 5L configuration, actually respond with a clear energy loss in the deep HIS simulation (Fig. 10, center column). The loss is compensated during the RCP scenario warming. An example is shown for a grid point at western US, where cooling trends take place in the HIS period (Fig. 11a,b) that expand below the 5th layer after 1900. The effect of the deep LSM is a damping of the cooling in the shallow LSM with a relatively warmer simulation (Fig. 11c) during the HIS period. During this interval, there is a net energy loss (Fig. 10, center) that gives way to warming in the 21st century, and a relatively cooler deep LSM simulation in the top layers below the surface (Fig. 11c).

In the scenario simulations, the deep BBCP induces a massive uptake of energy by the soil. The energy can increase by a factor of up to 5 in some regions compared to the shallow model. The

pattern of heat storage is very similar to that of HIS in the deep LSM configuration, with the regions showing small or negative energy storage, i.e. energy loss, now showing lower energy storage in the 21st century. In RCP2.6 values in the range of $15-30\cdot10^5 Jm^{-2}yr^{-1}$ are widespread with the highest values in northern Eurasia peaking above $30\cdot10^5 Jm^{-2}yr^{-1}$. In turn, values in the range of $30-45\cdot10^5 Jm^{-2}yr^{-1}$ are widespread in RCP4.5 over northern Eurasia and North America. Finally, RCP8.5 scales up over many regions with values in the range of $45-60\cdot10^5 Jm^{-2}yr^{-1}$ and above $60\cdot10^5 Jm^{-2}yr^{-1}$ in the northernmost latitudes. Overall, the changes associated to increasing the depth of the BBCP are far more important for energy storage than the differences related to scenario simulations in a shallow BBCP (González-Rouco et al. 2009).

Figure 12 (top) shows the comparison of the global amount of energy storage for the HIS and RCP simulations *vs.* depth with stepwise increases in the number of layers from the 5L to the 12L LSM. As in the case of temperature changes in Figure 9, storage saturates after reaching layer 9. It is interesting to note that the pace of increase for HIS and scenario simulations is very similar within the bounds of each scenario. Notice the different scales for HIS and the three RCPs. For most regions in Figure 10, increasing the depth of the BBCP translates in 1.5 times more heat stored in RCP4.5 than in RCP2.6 and a factor of more than 2.5 between RCP8.5 and RCP2.6. These factors agree with the ratio of ranges in the color scales in Figure 12 (top).

Figure 12 (bottom) expands the comparison of the 5L-shallow and 12L-deep BBCP configurations to different latitudinal bands. It becomes clear that the differences induced by expanding the depth of the BBCP exceed those related to changing the scenario within the shallow model configuration for all regions. If the RCP8.5 scenario is considered, changes for the comparison of the deep vs shallow LSM are larger for every region than the differences between different scenarios in the 12L configuration. As expected, the NH high latitudes indicate the largest heat storage in the deep model configuration. The lowest is attained for the SH mid and high latitudes. It is worth

noting that the saturation of energy storage in the shallow model induces negligible differences among regions. In fact, the least energy storage rate of the deep model at a regional scale exceeds the maximum rate of the shallow model of $5 - 10 \cdot 10^5 Jm^{-2}yr^{-1}$.

Global and regional estimates of AHCC, as well as cumulative heat uptake (CHU) in the 5L and 12L LSM configurations are provided in Table 2. Maximum values are reached in the northern high latitudes between 60N−90N with $97.0 \cdot 10^5 Jm^{-2}yr^{-1}$ for the deep model under RCP8.5. For these regions the AHCC exceeds the global mean by more than 25% in both, the shallow and the deep model configurations. The arguments raised for the comparison of the shallow *vs* deep LSM for different latitudinal bands and scenarios also apply in the numbers of Table 2. Consistent with previous figures, the smallest values for each RCP are attained at the SH mid and high latitudes. For RCP8.5 the deep model configuration produces between 4.4 and 10.4 times larger AHCC than the shallow one. Yet, while RCP8.5 AHCC values are larger than those of the other RCPs, the ratios of the deep *vs* shallow model variant are systematically larger for the RCP4.5 and RCP2.6 than for the RCP8.5 at each region. For instance, at NH high latitudes in the RCP8.5 scenario, the deep model accumulates about 5 times larger AHCC than the shallow version, whereas in the RCP4.5 and RCP2.6 ratios of 7.5 and 11.6 are attained, respectively. Ratios for the HIS simulations range across the various latitudinal regions between 2.3 and 4.5 times larger AHCC for the deep than the shallow variants. During HIS, values are comparable for the AHCC to those of MacDougall et al. (2008) from simulations with a 1-dimensional LSM driven by output of historical and SRES A2 climate scenarios of the ECHO-G GCM that rendered a global mean AHCC of $70.8 \cdot 10^5 Jm^{-2}yr^{-1}$ compared to our $69.5 \cdot 10^5 Jm^{-2}yr^{-1}$ with the RCP8.5 scenario (Tab. 2). For CHU, values of 1.2 and $6.7 \cdot 10^8 Jm^{-2}$ in RCP8.5 for the shallow and deep cases are also comparable with those reported by González-Rouco et al. (2009) of 1.3 and $6.5 \cdot 10^8 Jm^{-2}$, respectively. Hermoso de Mendoza et al. (2020) report values comparing the shallow version of the CLM4.5 LSM (Oleson et al. 2013,

42.1 m) and an expanded version reaching 342.1 m. In simulations of the $1900-2100$ AD period estimates render values of 2.9 and 5.2 $\cdot 10^8 Jm^{-2}$, respectively, thus somewhat smaller than the previously discussed values. This is consistent with their model showing lower climate sensitivity than the MPI-ESM (Meehl et al. 2020). Recent observational estimates of CHU (Cuesta-Valero et al. 2020) obtain values of 27 ZJ (*i.e.* $27 \cdot 10^{21} J$) since 1850 AD, that render an estimate of 12.1 $\cdot 10^5 Jm^{-2} yr^{-1}$; therefore larger than the HIS values obtained with the deep LSM (8.0 $\cdot 10^5 Jm^{-2} yr^{-1}$) and much larger than the 2.0 $\cdot 10^5 Jm^{-2} yr^{-1}$ of the shallow model variant. Since the 1960s heat accumulation estimated from observations is of the order of 12 ZJ, argued by von Schuckmann et al. (2020) to account for about 6 % of the total heat storage inventory of the Earth System.

3. Conclusions

This work addresses the model response of simulated subsurface temperatures and land energy storage when the BBCP is deepened in the JSBACH LSM under piControl, historical and RCP scenarios. This is done by driving the LSM by atmospheric prescribed conditions. The BBCP is deepened by a stepwise increase of the number of layers from 5 to 12, with exponentially growing thickness. This expands the depth of the LSM from its standard depth of 9.83 m down to a depth of 1417 m that allows for virtually detaching the BBCP from the surface. This evaluation focuses specifically on addressing model sensitivity. Comparison to observational datasets will be considered in future work.

The 500 year PIC simulations show that the initial state is important for the soil model. Soil temperature drifts in these runs can be of $1-2K$ in high latitude regions (60°N–90°N) and adjustments need longer timescales for the deepest layers. A length of 500 years is pertinent for the simulations developed herein, but this may depend on the initial conditions. Unrealistic

warming in the PIC equilibrium state due to the recycling of the 28-year boundary condition interval (Sapriza-Azuri et al. 2018) from pre-industrial conditions can be excluded here since the boundary conditions do not have any warming trends. Additionally, results show that the subsurface thermal regime is not equally set in every region and NH high latitude regions require longer timescales to reach equilibrium. Considering these issues is of importance for the development of coupled runs involving the atmosphere and ocean components that demand more computational resources. One strategy may be to use the equilibrium state produced with such stand-alone LSM simulations before hand. However, since the model equilibrium state in a coupled mode can differ from that of the stand-alone simulations some adjustment time may still be required.

The largest warming is attained in the RCP8.5 simulations and scales down when we consider other RCPs or the historical simulations. In these simulations, warming starts during the second half of the 20th century and intensifies in the RCPs. The range of warming for the top soil layers in the last three decades of the 21st century relative to pre-industrial conditions is of 6 K in RCP8.5, 3K in RCP4.5 and 2K in RCP2.6. The few first meters of the ground warm at very similar rates in line with what is shown by Soong et al. (2020), although the numbers here could change in coupled simulations, in which changes in soil temperatures can influence the surface energy balance. Deepening the BBCP produces a damping of the warming, i.e. a relative cooling, in the first 10 m of the ground that reaches 0.9 K for the 5th layer for RCP8.5 at global scales. This indicates an overestimation close to the surface (upper 10 m) in LSMs with shallow BBCPs, which results in erroneous soil-column thermal states and fluxes. The large influence is seen for the 4th and 5th layers and the impact is smaller for the first thin soil layers. This can also be influenced by the strong lead of the imposed surface boundary conditions and change in coupled model simulations; an issue that will be addressed in subsequent work. The relative cooling is widespread and it has a larger impact at higher latitudes, where it is larger than 1.5 K in the RCP8.5

locally. This enhanced response is expected from polar amplification (Holland and Bitz 2003; Bekryaev et al. 2010; Melo-Aguilar et al. 2018; Soong et al. 2020) as air temperatures at high latitudes are predicted to increase significantly faster than those in lower latitudes owing to thawing and ice albedo feedbacks. High latitude soils have a slower pace for warming but warm more than everywhere else. The inclusion of the deeper BBCP cools the top layers below the surface. Despite the relevance of soil temperature for Earth's carbon and energy budgets, ecosystem dynamics, food production or permafrost thermodynamics, studies of climate change impacts on soil processes, including surface and subsurface hydrology have mainly relied on air temperatures assuming they are accurate proxies for soil temperatures. Air warming is not necessarily a good proxy for soil warming in cold regions where snow and ice impede the direct transfer of sensible heat from the atmosphere to the soil (Melo-Aguilar et al. 2018; Soong et al. 2020) and the inclusion of deeper BBCPs may have a more clear impact on differenciating simulated subsurface from air temperature long-term responses, particularly at NH high latitudes. Additionally, the changes in the subsurface thermal structure reported herein may have implications for the hydrological state at the surface and below, particularly in the context of the hydro thermal physics discussed in Part II (Steinert et al. 2021).

Therefore, results indicate that the model depth of 10 m is insufficient for a proper representation of subsurface thermodynamics and a deeper BBCP is required to mitigate simulation errors to an acceptable amount. The effects of lowering the BBCP reach significantly the 8th model layer, with a depth at 91.73 m, and minimally the 9th layer (183.66 m) in our configuration. Thus a minimum depth of 100 m is needed for historical and RCP simulations to account for a realistic role of the land model, thereby much deeper than that in current CMIP5 and CMIP6 ESM schemes (Cuesta-Valero et al. 2016; Burke et al. 2020). The additional layers reaching a depth of 1417 m should make our model configuration potentially suitable for longer simulations like the *past1000*

last millenium experiments (Jungclaus et al. 2017) in which lowering the depth of the BBCP may have an impact on low frequency variability. Indeed, the effect of the deep model on long-term variability will be to compensate warming (cooling) periods with relative cooling (warming) of the layers near the subsurface as shown herein.

Terrestrial energy storage in the deep LSM is between 3 and 5 times larger than in the shallow LSM. As in the case of subsurface temperature, changes saturate after including the 9th layer. The range of energy storage is very small for the shallow model and any of the RCP scenarios with the deep model peaks higher than the shallow RCP8.5 simulation. Increasing land depth produces a larger impact than changes in RCPs and the impact is larger for the NH latitude regions, where the largest temperature increases occur. Simulated values compare well to previous assessments with stand-alone LSM simulations under historical and scenario conditions. Even for the deep LSM, values are somewhat smaller than the recent evaluation of land heat storage by Cuesta-Valero et al. (2020) using observed borehole temperature profiles, although consistent with the fact that MPI-ESM simulates somewhat smaller temperatures than observed (Stevens et al. 2013).

The energy that is not stored in the soil in shallow BBCP models is assumed to be transferred to somewhere else into other Earth's subsystems. Although the soil layers close to the surface experience a cooling when deepening the BBCP, the overall increase in terrestrial energy uptake will likely affect land-air interactions. The model internal energy distribution may change to a larger net energy contribution from the soil, which increases the importance of the land system in climate change coupled model simulations. Additionally, the geothermal heat flux (GHF) may have some contribution to the subsurface thermal state within the expanded soil depths. Traditionally, it has not been considered as LSMs are usually shallow enough so that the influence of the GHF diminishes. A recent study by Hermoso de Mendoza et al. (2020) shows that in a model with

a depth of 340 m, the GHF has only little effect. These issues will be addressed in future work assessing coupled simulations with the JSBACH model.

Acknowledgments. Thanks to R. Schnur and V. Gayler from MPI Hamburg. We gratefully acknowledge the IlModels (CGL2014-59644-R) and GreatModelS (RTI2018-102305-B-C21) projects funded by the Spanish MINECO. SH contributed in the frame of the ERANET-plus-Russia project SODEEP (Study Of the Development of Extreme Events over Permafrost areas) supported by BMBF (Grant no. 01DJ18016A). This work used resources of the Deutsches Klimarechenzentrum (DKRZ) granted by its Scientific Steering Committee (WLA) under project ID bm1026.

Data availability statement. The JSBACH simulation data and soil parameter datasets used in this study are available from the corresponding authors upon reasonable request. They are available at the servers of the Deutsches Klimarechenzentrum (DKRZ) and need to be granted access by the authors and the DKRZ.

References

Alexeev, V. A., D. J. Nicolsky, V. E. Romanovsky, and D. M. Lawrence, 2007: An evaluation of deep soil configurations in the clm3 for improved representation of permafrost. *Geophysical Research Letters*, **34 (9)**, doi:10.1029/2007GL029536.

Bekryaev, R. V., I. V. Polyakov, and V. A. Alexeev, 2010: Role of polar amplification in long-term surface air temperature variations and modern arctic warming. *Journal of Climate*, **23 (14)**, 3888–3906, doi:10.1175/2010JCLI3297.1.

669 Beltrami, H., E. Bourlon, L. Kellman, and J. F. González-Rouco, 2006: Spatial pat-
670 terns of ground heat gain in the northern hemisphere. *Geophys. Res. Lett.*, **33**, L06 717,
671 doi:10.1029/2006GL025 676.

672 Bonan, G. B., and S. C. Doney, 2018: Climate, ecosystems, and planetary futures: The challenge
673 to predict life in earth system models. *Science*, **359**, eaam8328, DOI: 10.1126/science.aam8328.

674 Bonan, G. B., E. G. Patton, I. N. Harman, K. W. Oleson, J. J. Finnigan, Y. Lu, and E. A. Burakowski,
675 2018: Modeling canopy-induced turbulence in the earth system: a unified parameterization of
676 turbulent exchange within plant canopies and the roughness sublayer (clm-ml v0). *Geosci. Model*
677 *Dev.*, **11**, 1467–1496, DOI: 10.5194/gmd–11–1467–2018.

678 Brovkin, V., L. Boysen, T. Raddatz, V. Gayler, A. Loew, and M. Claussen, 2013: Evaluation of
679 vegetation cover and land-surface albedo in mpi-esm cmip5 simulations. *Journal of Advances*
680 *in Modeling Earth Systems*, **5 (1)**, 48–57, doi:10.1029/2012MS000169.

681 Brovkin, V., T. Raddatz, C. H. Reick, M. Claussen, and V. Gayler, 2009: Global biogeophysical
682 interactions between forest and climate. *Geophysical Research Letters*, **36 (7)**, doi:10.1029/
683 2009GL037543.

684 Burke, E. J., Y. Zhang, and G. Krinner, 2020: Evaluating permafrost physics in the coupled
685 model intercomparison project 6 (cmip6) models and their sensitivity to climate change. *The*
686 *Cryosphere*, **14 (9)**, 3155–3174, doi:10.5194/tc-14-3155-2020, URL https://tc.copernicus.org/
687 articles/14/3155/2020/.

688 Carslaw, H. S., and J. C. Jaeger, 1959: *Conduction of heat in solids*. 3rd ed., Oxford Univ. Press.
689 2nd ed., New York.

690 Craig, A., S. Valcke, and L. Coquart, 2017: Development and performance of a new version
691 of the oasis coupler, oasis3-mct_3.0. *Geoscientific Model Development*, **10 (9)**, 3297–3308,
692 doi:10.5194/gmd-10-3297-2017.

693 Crowley, T. J., and T. S. Lowery, 2000: How warm was the medieval warm period. *Ambio*, **29**,
694 51–54.

695 Cubasch, U., D. Wuebbles, D. Chen, M. C. Facchini, D. Frame, N. Mahowald, and J. G. Winther,
696 2013: *Introduction*. Cambridge University Press, Cambridge, United Kingdom and New York,
697 NY, USA.

698 Cuesta-Valero, F. J., A. García-García, H. Beltrami, J. F. González-Rouco, and E. García-
699 Bustamante, 2020: Long-term global ground heat flux and continental heat storage from geother-
700 mal data. *Climate of the Past Discussions*, **2020**, 1–27, doi:10.5194/cp-2020-65.

701 Cuesta-Valero, F. J., A. García-García, H. Beltrami, and J. E. Smerdon, 2016: First assessment
702 of continental energy storage in cmip5 simulations. *Geophysical Research Letters*, **43 (10)**,
703 5326–5335, doi:10.1002/2016GL068496.

704 de Vrese, P., T. Stacke, and S. Hagemann, 2018: Exploring the biogeophysical limits of global food
705 production under different climate change scenarios. *Earth System Dynamics*, **9 (2)**, 393–412,
706 doi:10.5194/esd-9-393-2018.

707 Dümenil, L., and E. Todini, 1992: Chapter 9 - a rainfall-runoff scheme for use in the hamburg
708 climate model. *Advances in Theoretical Hydrology, a Tribute to J. Dooge. European Geophysical*
709 *Society Series on Hydrological Sciences*, 129–157, doi:10.1016/B978-0-444-89831-9.50016-8.

Dunne, K. A., and C. J. Willmott, 1996: Global distribution of plant-extractable water capacity of soil. *International Journal of Climatology*, **16 (8)**, 841–859, doi:10.1002/(SICI)1097-0088(199608)16:8<841::AID-JOC60>3.0.CO;2-8.

Ekici, A., C. Beer, S. Hagemann, J. Bolke, M. Langer, and C. Hauck, 2014: Simulating the high-latitude permafrost regions by the jsbach terrestrial ecosystemmodel. *Geosci. Model Dev.*, **7**, 631–647.

Eyring, V., S. Bony, G. A. Meehl, C. A. Senior, B. Stevens, R. J. Stouffer, and K. E. Taylor, 2016: Overview of the coupled model intercomparison project phase 6 (cmip6) experimental design and organization. *Geosci. Model Dev.*, **9**, 1937–1958, doi:10.5194/gmd–9–1937–2016.

Flato, G., and Coauthors, 2013: *Evaluation of climate models. In: Climate Change 2013: The Physical Science Basis. Contribution of Working Group I to the Fifth Assessment Report of the Intergovernmental Panel on Climate Change*. Cambridge University Press, Cambridge, United Kingdom and New York, NY, USA.

Gao, C. C., A. Robock, and C. Ammann, 2008: Volcanic forcing of climate over the past 1500 years: an improved ice core-based index for climate models. *J. Geophys. Res.*, **113**, D23 111, doi: 10.1029/2008JD010 239.

Giorgetta, M. A., and Coauthors, 2013: Climate and carbon cycle changes from 1850 to 2100 in mpi-esm simulations for the coupled model intercomparison project phase 5. *Journal of Advances in Modeling Earth Systems*, **5 (3)**, 572–597, doi:10.1002/jame.20038, URL http://dx.doi.org/10.1002/jame.20038.

Goll, D. S., V. Brovkin, J. Liski, T. Raddatz, T. Thum, and K. E. O. Todd-Brown, 2015: Strong dependence of co2 emissions from anthropogenic land cover change on initial land cover and

soil carbon parametrization. *Global Biogeochemical Cycles*, **29 (9)**, 1511–1523, doi:10.1002/2014GB004988.

González-Rouco, J. F., H. Beltrami, E. Zorita, and B. Stevens, 2009: Borehole climatology: a discussion based on contributions from climate modelling. *Clim. Past*, **5**, 99–127.

González-Rouco, J. F., H. Beltrami, E. Zorita, and H. von Storch, 2006: Simulation and inversion of borehole temperature profiles in surrogate climates: Spatial distribution and surface coupling. *Geophys. Res. Lett.*, **33**, L01 703,doi:10.1029/2005GL024 693.

Guo, Z., and Coauthors, 2006: Glace: The global land-atmosphere coupling experiment. part ii: Analysis. *Journal of Hydrometeorology*, **7 (4)**, 611–625, doi:10.1175/JHM511.1.

Hagemann, S., T. Blome, A. Ekici, and C. Beer, 2016: Soil-frost-enabled soil-moisture-precipitation feedback over northern high latitudes. *Earth Syst. Dynam.*, **7**, 611–625, doi:10.5194/esd–7–611–2016.

Hagemann, S., A. Loew, and A. Andersson, 2013: Combined evaluation of mpi-esm land surface water and energy fluxes. *J. Adv. Model. Earth Systems*, **5**, 259–286, DOI: 10.1029/2012MS000 173.

Hagemann, S., and S. Stacke, 2015: Impact of the soil hydrology scheme on simulated soil moisture memory. *Clim. Dyn*, **44**, 17 319–1750, DOI: 10.1007/s00 382–014–2221–6.

Hagemann, S., T. Stacke, and H. T. M. Ho-Hagemann, 2020: High resolution discharge simulations over europe and the baltic sea catchment. *Front. in Earth Sci.*, **8**, 12, doi: 10.3389/feart.2020.00 012.

Hansen, J., M. Sato, P. Kharecha, and K. von Schuckmann, 2011: Earth's energy imbalance and implications. *Atmospheric Chemistry and Physics*, **11 (24)**, 13 421–13 449, doi:10.5194/acp-11-13421-2011.

Hansen, J., and Coauthors, 2005: Earth's energy imbalance: confirmation and implications. *Science*, **308**, 1431–1435.

Heidkamp, M., A. Chlond, and F. Ament, 2018: Closing the energy balance using a canopy heat capacity and storage concept – a physically based approach for the land component jsbachv3.11. *Geoscientific Model Development*, **11 (8)**, 3465–3479, doi:10.5194/gmd-11-3465-2018.

Hermoso de Mendoza, I., H. Beltrami, A. H. MacDougall, and J.-C. Mareschal, 2020: Lower boundary conditions in land surface models - effects on the permafrost and the carbon pools: a case study with clm4.5. *Geosci. Model. Dev.*, **13**, 1663–1683, dOI: 10.5194/gmd-13-1663-2020.

Holland, M. M., and C. M. Bitz, 2003: Polar amplification of climate change in coupled models. *Climate Dynamics*, **21**, 221–232, https://doi.org/10.1007/s00 382–003–0332–6.

Huang, J., 2016: Effects of soil temperature and snow cover on the mortality of overwintering pupae of the cotton bollworm, helicoverpa armigera (hübner) (lepidoptera: Noctuidae). *I. J. Biometeorol.*, **60**, 977–989 DOI: 10.1007/s00 484–015–1090–y.

Ilyina, T., K. D. Six, J. Segschneider, E. Maier-Reimer, H. Li, and I. Núñez-Riboni, 2013: Global ocean biogeochemistry model hamocc: Model architecture and performance as component of the mpi-earth system model in different cmip5 experimental realizations. *Journal of Advances in Modeling Earth Systems*, **5 (2)**, 287–315, doi:10.1029/2012MS000178.

Jungclaus, J. H., and Coauthors, 2013: Characteristics of the ocean simulations in the max planck institute ocean model (mpiom) the ocean component of the mpi-earth system model. *Journal of Advances in Modeling Earth Systems*, **5 (2)**, 422–446, doi:10.1002/jame.20023.

Jungclaus, J. H., and Coauthors, 2017: The pmip4 contribution to cmip6 – part 3: The last millennium, scientific objective, and experimental design for the pmip4 *past1000* simulations. *Geoscientific Model Development*, **10 (11)**, 4005–4033, doi:10.5194/gmd-10-4005-2017.

Knutti, R., M. A. A. Rugenstein, and G. C. Hegerl, 2017: Beyond equilibrium climate sensitivity. *Nature Geoscience*, **10**, 727–744, DOI: 10.1038/NGEO3017.

Koster, R. D., and Coauthors, 2006: Glace: The global land-atmosphere coupling experiment. part i: Overview. *Journal of Hydrometeorology*, **7 (4)**, 590–610, doi:10.1175/JHM510.1.

Krinner, G., and Coauthors, 2018: Esm-snowmip: assessing snow models and quantifying snow-related climate feedbacks. *Geoscientific Model Development*, **11 (12)**, 5027–5049, doi:10.5194/gmd-11-5027-2018.

Lawrence, D. M., A. G. Slater, V. E. Romanovsky, and D. J. Nicolsky, 2008: Sensitivity of a model projection of near-surface permafrost degradation to soil column depth and representation of soil organic matter. *J. Geophys. Res.*, **113**, F02 011, DOI:10.1029/2007JF000 883.

Lawrence, D. M., and Coauthors, 2011: Parameterization improvements and functional and structural advances in version 4 of the community land model. *J. Adv. Model. Earth Syst.*, **33**, M03 001, oi:10.1029/2005GL025 080.

Lawrence, D. M., and Coauthors, 2019: The community land model version 5: Description of new features, benchmarking, and impact of forcing uncertainty. *J. Adv. Model. Earth Systems*, **11**, 4245–4287. doi: 10.1029/2018MS001 583.

Lawrence, P. J., and Coauthors, 2012: Simulating the biogeochemical and biogeophysical impacts of transient land cover change and wood harvest in the community climate system model (ccsm4) from 1850 to 2100. *Journal of Climate*, **25 (9)**, 3071–3095, doi:10.1175/JCLI-D-11-00256.1.

Levitus, S., and Coauthors, 2012: World ocean heat content and thermosteric sea level change (0-2000 m), 1955-2010. *Geophysical Research Letters*, **39 (10)**, doi:10.1029/2012GL051106.

Lynch-Stieglitz, M., 1994: The development and validation of a simple snow model for the giss gcm. *J. Clim.*, **7**, 1842–1855.

MacDougall, A. H., H. Beltrami, J. F. González-Rouco, M. B. Stevens, and E. Bourlon, 2010: Comparison of observed and general circulation model derived continental sub-surface heat flux in the northern hemisphere. *J. Geophys. Res.*, **115**, D12 109, doi:10.1029/ 2009JD013 170.

MacDougall, A. H., J. F. González-Rouco, M. B. Stevens, and H. Beltrami, 2008: Quantification of subsurface heat storage in a gcm simulation. *Geophys. Res. Lett.*, **35**, L13 702, doi:10.1029/2008GL034 639.

Mareschal, J. C., and H. Beltrami, 1992: Evidence for recent warming from perturbed thermal gradients: examples from eastern canada. *Clim. Dyn.*, **6**, 135–143.

Masson-Delmotte, V., and Coauthors, Eds., 2018: *Summary for Policymakers*, In: Global Warming of 1.5°*C*. An IPCC Special Report on the impacts of global warming of 1.5°*C* above pre-industrial levels and related global greenhouse gas emission pathways, in the context of strengthening the global response to the threat of climate change, sustainable development, and efforts to eradicate poverty., Cambridge University Press, Cambridge, United Kingdom and New York, NY, USA.

Mauritsen, T., and Coauthors, 2019: Developments in the mpi-m earth system model version 1.2 (mpi-esm1.2) and its response to increasing co2. *Journal of Advances in Modeling Earth Systems*, **11 (4)**, 998–1038, doi:10.1029/2018MS001400.

McGuffie, K., and A. Henderson-Sellers, 2005: *A Climate Modelling Primer*. 3rd ed., john Wiley and Sons, Ltd.

McGuire, A. D., and Coauthors, 2018: Dependence of the evolution of carbon dynamics in the northern permafrost region on the trajectory of climate change. *PNAS*, **115 (15)**, 3882–3887, DOI: 10.1073/pnas.1719903 115, doi:10.1073/pnas.1719903115.

Meehl, G. A., C. A. Senior, V. Eyring, G. Flato, J.-F. Lamarque, R. J. Stouffer, K. E. Taylor, and M. Schlund, 2020: Context for interpreting equilibrium climate sensitivity and transient climate response from the cmip6 earth system models. *Science Advances*, **6 (26)**, doi:10.1126/sciadv. aba1981.

Melo-Aguilar, C., J. F. González-Rouco, E. García-Bustamante, J. Navarro-Montesinos, and N. Steinert, 2018: Influence of radiative forcing factors on ground–air temperature coupling during the last millennium: implications for borehole climatology. *Climate of the Past*, **14 (11)**, 1583–1606, doi:10.5194/cp-14-1583-2018.

Nabel, J. E. M. S., K. Naudts, and J. Pongratz, 2020: Accounting for forest age in the tile-based dynamic global vegetation model jsbach4 (4.20p7; git feature/forests) – a land surface model for the icon-esm. *Geoscientific Model Development*, **13 (1)**, 185–200, doi:10.5194/gmd-13-185-2020.

Oleson, K. W., and Coauthors, 2010: Technical description of version 4.0 of the community land model (clm). Tech. Rep. 478+STR, doi:10.5065/D6FB50WZ, NCAR, Boulder, Colorado.

Oleson, K. W., and Coauthors, 2013: Technical description of version 4.5 of the community land model (clm). Tech. Rep. 503+STR, doi:10.5065/D6RR1W7M, NCAR, Boulder, Colorado.

Oreskes, N., K. Shrader-Frechette, and K. Belitz, 1994: Verification, validation, and confirmation of numerical models in the earth sciences. *Science*, **263**, 641–646.

Ortega, P., M. Montoya, F. González-Rouco, H. Beltrami, and D. Swingedouw, 2013: Variability of the ocean heat content during the last millennium - an assessment with the echo-g model. *Climate of the Past*, **9 (2)**, 547–565, doi:10.5194/cp-9-547-2013.

Otto-Bliesner, B., and Coauthors, 2016: Climate variability and change since 850 c.e.: An ensemble approach with the community earth system model (cesm). *BAMS*, **97 (5)**, 735–754, doi:10.1175/BAMS-D-14-00233.1.

Pachauri, R. K., and L. A. Mayer, Eds., 2014: *Climate Change 2014: Synthesis Report. Contribution of Working Groups I, II and III to the Fifth Assessment Report of the Intergovernmental Panel on Climate Change*, Geneva, Switzerland, 151 pp.

Palmer, T., and B. Stevens, 2019: The scientific challenge of understanding and estimating climate change. *PNAS*, **116**, 24 390–24 395, DOI: 10.1073/pnas.1906691 116.

Phillips, C. L., 2020: How much will soil warm? *Journal of Geophysical Research: Biogeosciences*, **125**, e2020JG005 668, doi:10.1029/2020JG005668.

Pollack, H. N., and S. Huang, 2000: Climate reconstruction from subsurface temperatures. *Annu. Rev. Earth. Planet. Sci.*, **28**, 339–365.

Pollack, H. N., J. E. Smerdon, and P. E. van Keken, 2005: Variable seasonal coupling between air and ground temperatures: a simple representation in terms of subsurface thermal diffusivity. *Geophys. Res. Lett.*, **32**, doi:10.1029/2005GL023 869.

Raddatz, T. J., and Coauthors, 2007: Will the tropical land biosphere dominate the climate-carbon cycle feedback during the twenty-first century? *Clim. Dyn.*, **29**, 565–574, DOI: 10.1007/s00 382–007–0247–8.

Reick, C. H., T. Raddatz, V. Brovkin, and V. Gayler, 2013: Representation of natural and anthropogenic land cover change in mpi-esm. *Journal of Advances in Modeling Earth Systems*, **5 (3)**, 459–482, doi:10.1002/jame.20022.

Rhein, M., and Coauthors, 2013: *Observations: Ocean. In: Climate Change 2013: The Physical Science Basis. Contribution of Working Group I to the Fifth Assessment Report of the Intergovernmental Panel on Climate Change*. Cambridge University Press, Cambridge, United Kingdom and New York, NY, USA.

Roeckner, E., L. Dümenil, E. Kirk, F. Lunkeit, M. Ponater, B. Rockel, R. Sausen, and U. Schlese, 1989: The hamburg version of the ecmwf model (echam). in *Research Activities in Oceanic and Atmospheric Modelling* (G. J. Boer (Ed.) CAS/JSC Working Group in Numerical Experimentation 13, World Meteorological Organization, Geneva, Switzerland.

Roeckner, E., and Coauthors, 1992: Simulation of the present day climate with the echam model: Impact of model physics and resolution. Tech. Rep. 93, Max-Planck-Institut füer Meteorologie, Hamburg, Germany.

Roeckner, E., and Coauthors, 2003: The atmospheric general circulation model echam5. part i: Model description. Tech. Rep. 349, Max-Planck-Institut fuer Meterologie, Hamburg.

Sapriza-Azuri, G., P. Gamazo, S. Razavi, and H. S. Wheater, 2018: On the appropriate definition of soil profile configuration and initial conditions for land surface–hydrology

models in cold regions. *Hydrology and Earth System Sciences*, **22 (6)**, 3295–3309, doi: 10.5194/hess-22-3295-2018.

Schulz, J.-P., L. Dümenil, and J. Polcher, 2001: On the land surface-atmosphere coupling and its impact in a single-column atmospheric model. *Journal of Applied Meteorology*, **40 (3)**, 642–663, doi:10.1175/1520-0450(2001)040<0642:OTLSAC>2.0.CO;2.

Seneviratne, S. I., T. Corti, E. L. Davin, M. Hirschi, E. B. Jaeger, I. Lehner, B. Orlowsky, and A. J. Teuling, 2010: Investigating soil moisture-climate interactions in a changing climate: A review. *Earth-Science Reviews*, **99 (3)**, 125 – 161, doi:https://doi.org/10.1016/j.earscirev.2010.02.004.

Simpkins, G., 2017: Progress in climate modelling. *Nature Climate Change*, **7**, 684–685.

Smerdon, J. E., and M. Stieglitz, 2006: Simulating heat transport of harmonic temperature signals in the earth's shallow subsurface: lower-boundary sensitivities. *Geophys. Res. Lett.*, **33**, L14 402, doi: 10.1029/2006GL026 816.

Soong, J. L., C. L. Phillips, C. Ledna, C. D. Koven, and M. S. Torn, 2020: Cmip5 models predict rapid and deep soil warming over the 21st century. *Journal of Geophysical Research: Biogeosciences*, **125 (2)**, e2019JG005 266, doi:10.1029/2019JG005266.

Steinert, N. J., and Coauthors, 2021: Increasing the depth of a land surface model. part ii: Sensitivity to improved coupling between soil hydrology and thermodynamics and associated permafrost response. *J. Climate*, submitted.

Stevens, B., and Coauthors, 2013: Atmospheric component of the mpi-m earth system model: Echam6. *Journal of Advances in Modeling Earth Systems*, **5 (2)**, 146–172, doi:10.1002/jame.20015.

Stevens, M. B., J. E. Smerdon, J. F. González-Rouco, M. Stieglitz, and H. Beltrami, 2007: Effects of bottom boundary condition placement on subsurface heat storage: Implications for climate model simulations. *Geophysical Research Letters*, **34**, L02 702, doi:10.1029/2006GL028 546.

Stoica, P., and R. Moses, 1997: *Introduction to spectral analysis*. Prentice Hall.

Sun, S., and X. Zhang, 2004: Effect of the lower boundary position of the fourier equation on the soil energy balance. *Adv. Atmos. Sci.*, **21 (6)**, 868–878.

Taylor, K. E., R. J. Stouffer, and G. A. Meehl, 2012: An overview of cmip5 and the experiment design. *Bull. Amer. Meteor. Soc.*, **93**, DOI:10.1175/BAMS–D–11–00 094.1.

Trenberth, K. E., J. T. Fasullo, and J. Kiehl, 2009: Earth's global energy budget. *Bulletin of the Americal Meteorological Society*, **33**, 311–323, DOI:10.1175/2008BAMS2634.1.

Turcotte, D. E., and G. Schubert, 2002: *Geodynamics*. 2nd ed., Cambridge University Press.

van Genuchten, M. T., 1980: A closed-form equation for predicting the hydraulic conductivity of unsaturated soils. *Soil Science Society of America Journal*, **44 (5)**, 892–898, doi:10.2136/sssaj1980.03615995004400050002x.

von Schuckmann, K., and Coauthors, 2020: Heat stored in the earth system: Where does the energy go? the gcos earth heat inventory team. *Earth System Science Data Discussions*, **2020**, 1–45, doi:10.5194/essd-2019-255.

von Storch, H., 2010: Climate models and modeling: an editorial essay. *WIRESs Clim. Change*, **1**, 305–310. doi: 10.1002/wcc.12.

Warrilow, D. A., A. B. Sangster, and A. Slingo, 1986: Modelling of land surface processes and their influence on european climate. Tech. rep., Met. Of. Tech. Note 20 DCTN 38, Bracknell, UK.

Wu, D., S. Piao, Y. Liu, P. Ciais, and Y. Yao, 2018: Evaluation of cmip5 earth system models for the spatial patterns of biomass and soil carbon turnover times and their linkage with climate. *Journal of Climate*, **31 (15)**, 5947–5960, doi:10.1175/JCLI-D-17-0380.1.

Zhao, C., and Coauthors, 2017: Temperature increase reduces global yields of major crops in four independent estimates. *Proceedings of the National Academy of Sciences*, **114 (35)**, 9326–9331, doi:10.1073/pnas.1701762114.

LIST OF TABLES

942 TABLE 1. Number, thickness, and depth of the center and bottom boundary of each layer in JSBACH. Note
943 that layers 1 to 5, above the line separation, belong to the standard model version while layers 6 to 12 correspond
944 to the extension developed in this work.

Layer	Thickness (m)	Center (m)	Lower limit (m)
1	0.06	0.03	0.06
2	0.26	0.19	0.32
3	1.00	0.78	1.32
4	2.81	2.68	4.13
5	5.70	6.98	9.83
6	11.76	15.71	21.59
7	23.52	33.35	45.11
8	46.62	68.42	91.73
9	91.93	137.70	183.66
10	180.81	274.07	364.47
11	355.17	542.06	719.64
12	697.20	1068.24	1416.84

TABLE 2. Global and regional mean annual heat content change, AHCC [$10^5 Jm^{-2}yr^{-1}$] and mean global cumulative heat uptake, CHU [$10^8 Jm^{-2}$] in the shallow 5-layer (S) and deep 12-layer (D) LSM configuration for the historical (HIS) simulation and the RCP8.5 (RCP) simulation. AHCC values are shown for the NH high latitudes (NHhl), mid latitudes (NHml, SHml) and for intertropical low latitudes (Llat). Results for AHCC from MacDougall et al. (2008), MD2008, and for CHU from González-Rouco et al. (2009) and Hermoso de Mendoza et al. (2020), GR2009 and HM2020, are shown for comparison. Note that the forcing conditions used in our simulations are different from the ones used in MD2008 and GR2009, but can be compared to the RCP8.5 forcing simulations.

	AHCC										CHU	
	global		NHhl		NHml		Llat		SHml		global	
	S	D	S	D	S	D	S	D	S	D	S	D
HIS	2.0	8.0	3.5	8.1	1.8	6.3	1.8	8.2	1.2	4.3	0.3	1.2
RCP2.6	1.9	28.6	3.7	42.8	2.7	26.8	1.4	26.3	1.4	17.4	0.2	2.7
RCP4.5	4.7	41.3	7.7	57.6	4.9	38.3	4.6	38.7	3.6	27.9	0.5	4.0
RCP8.5	12.4	69.5	19.8	97.0	15.6	69.5	12.9	67.2	7.6	45.2	1.2	6.7
MD2008	11.4	70.8									-	-
GR2009	-	-									1.3	6.5
HM2020	-	-									2.9	5.2

LIST OF FIGURES

Soil temperature anomaly profiles for the last 30 years in the RCPs scenario ($\bar{T}_{2071-2100}$; dark shaded area) relative to the temperatures of the first soil level at the end of the piControl simulation ($\bar{T}_{1825-1850}$; dark shaded area) for the shallow 5L (f) the deep 12L configuration and (i) the differences between them for the first 5 model layers. For the RCP8.5, profiles are shown specifically also for several latitudinal bands for the (b) shallow, (e) deep and (h) for the differences. 52

Fig. 8. As Fig. 6 for different latitudinal bands (see legend): (a,b) NH high latitudes (60°N−90°N) and (c,d) intertropical regions (30°S−30°N). Note that, while the vertical scale is different for each latitudinal band, the temperature range is the same for each panel in order to make them comparable. 53

Fig. 9. (Top row) Subsurface temperature differences [K] between the end of the 21st century and the pre-industrial temperature ($\bar{T}_{2095-2100} - \bar{T}_{1850-1855}$) for the 5-layer shallow (x-axes) and 12-layer deep (y-axis) soil model configuration for various layers (colors) and latitudinal bands (symbols). Note that the y-axis temperatures cover different ranges. (Bottom row) Soil temperature differences [K] at layer 5 between LSMs with a given number of layers (x-axis) that progressively increase from 6 to 12 and the reference 5L configuration. Colors stand for the various latitudinal bands. 54

Fig. 10. (Left column) Annual heat content change [$10^5 Jm^{-2}yr^{-1}$] relative to piControl in the shallow 5L and (Middle column) deep 12L LSM configurations for the historical (1850 – 2005), the RCP2.6, RCP4.5 and RCP8.5 (2006 – 2100) simulations (row 1 to 4). (Right column) Annual heat content change [$10^5 Jm^{-2}yr^{-1}$] differences between the deep 12L and shallow 5L LSM configurations for each case. Polar ice sheets are not included. 55

Fig. 11. (a) Hovmöller diagram of the absolute temperatures [K] *vs.* depth [m] at a gridpoint in western US (45.7° N, 112.5° W) for the last 100 years in the piControl simulation (dates are arbitrary and do not correspond to actual dates in forcing in PIC) continued into the historical (1850 – 2005) and RCP8.5 (2006 – 2100) simulations for the 5L configuration, (c) the 12L configuration and (c) soil temperature differences (K) for the first 5 layers in between the deep 12L and the shallow 5L configurations. 56

Fig. 12. (Top) Global mean annual heat content change [$10^5 Jm^{-2}yr^{-1}$] in dependence to BBCP-depth configuration for HIS (left axis) and the RCP simulations (right axis). Results are shown for stepwise increases from the 5L to the 12L configuration. (Bottom) Area mean annual heat content change [$10^5 Jm^{-2}yr^{-1}$] in the shallow (circles) and deep (triangles) LSM configurations, for global, NH high latitudes, NH mid latitudes, intertropical regions, SH mid latitudes and SH high latitudes. 57

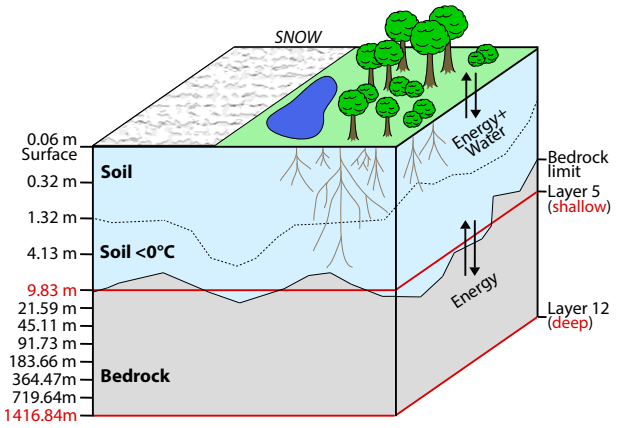

FIG. 1. Vertical structure of the JSBACH LSM version used herein. The scheme corresponds to an example of grid points with frozen soil and partial snow cover, e.g. in northern high latitudes; see also Steinert et al. (2021) for comparison. The numbers left of the soil column show the depths of the bottom of each layer. Red lines indicate the downward expansion of the BBCP with seven more layers.

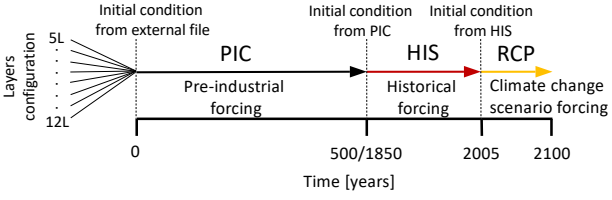

1037 FIG. 2. Experimental setup for the JSBACH simulations with gradually increasing layer configurations from 5 to
1038 12 layers ($5L-12L$) under pre-industrial, historical and 21^{st} century climate change (RCP) forcing scenarios. The
1039 pre-industrial control simulation (PIC) is performed for 500 years with conditions of 1850 to reach temperature
1040 equilibrium in the subsurface layers, before running the consecutive historical (HIS) and future scenario (RCP)
1041 simulations.

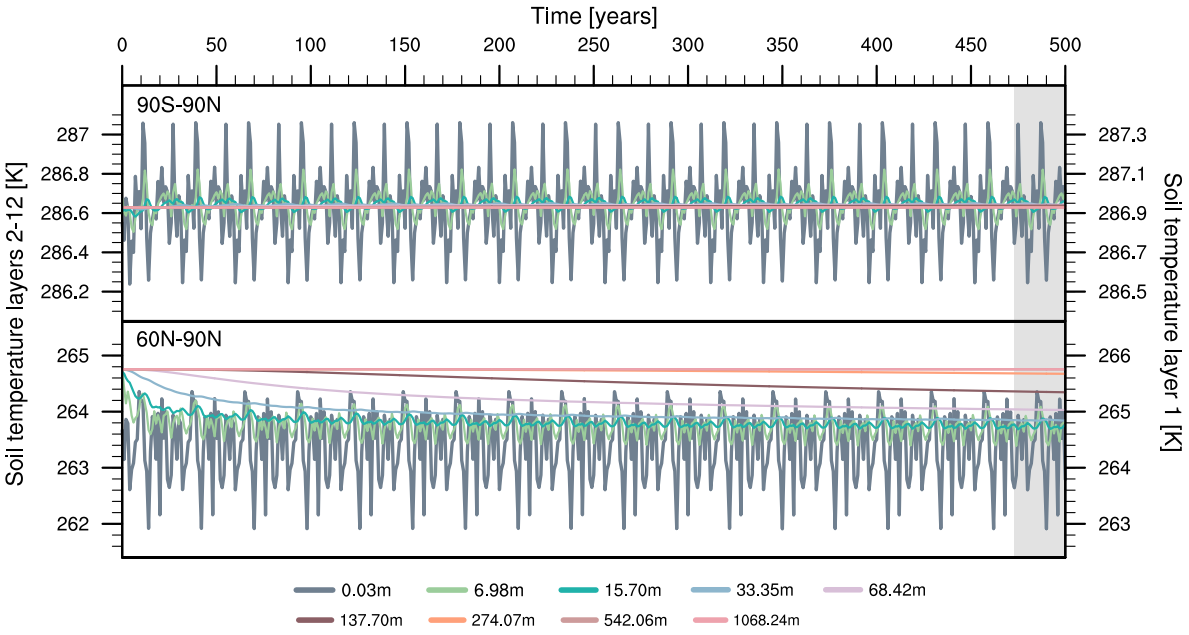

FIG. 3. (Top) Global and (Bottom) Northern Hemisphere high-latitude (60° N−90° N; bottom) subsurface temperature [K] in the 12L deep land surface model configuration in the PIC simulation of 500 years. The uppermost subsurface layer (solid grey) corresponds to the temperature scale on the right, all other layers correspond to the temperature scale on the left. The gray shaded area (years 473 – 500) corresponds to the last 28-year chunk of the driving boundary conditions (see text for details). Layers 2, 3 and 4 are not included to enhance visibility.

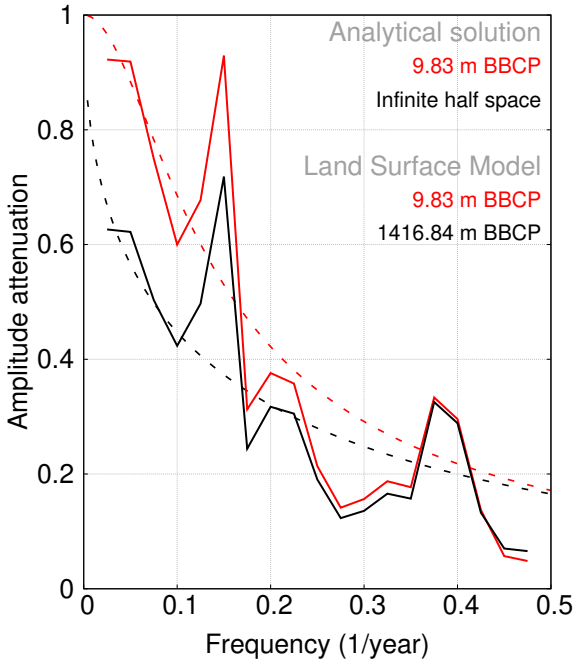

FIG. 4. Ratio of spectral amplitude estimates for the temperature time series at the first and fifth model layers using the shallow 5L (solid red) and 12L deep model (solid black) for a grid point at 27.0° N, 5.6° E. Spectral estimates have been obtained from the last 100 years in the piControl simulations using Welch's periodogram (Stoica and Moses 1997). Dashed lines correspond to analytical estimates of the conductive attenuation expected at each frequency for a 9.83 m shallow and an infinite half space (Smerdon and Stieglitz 2006).

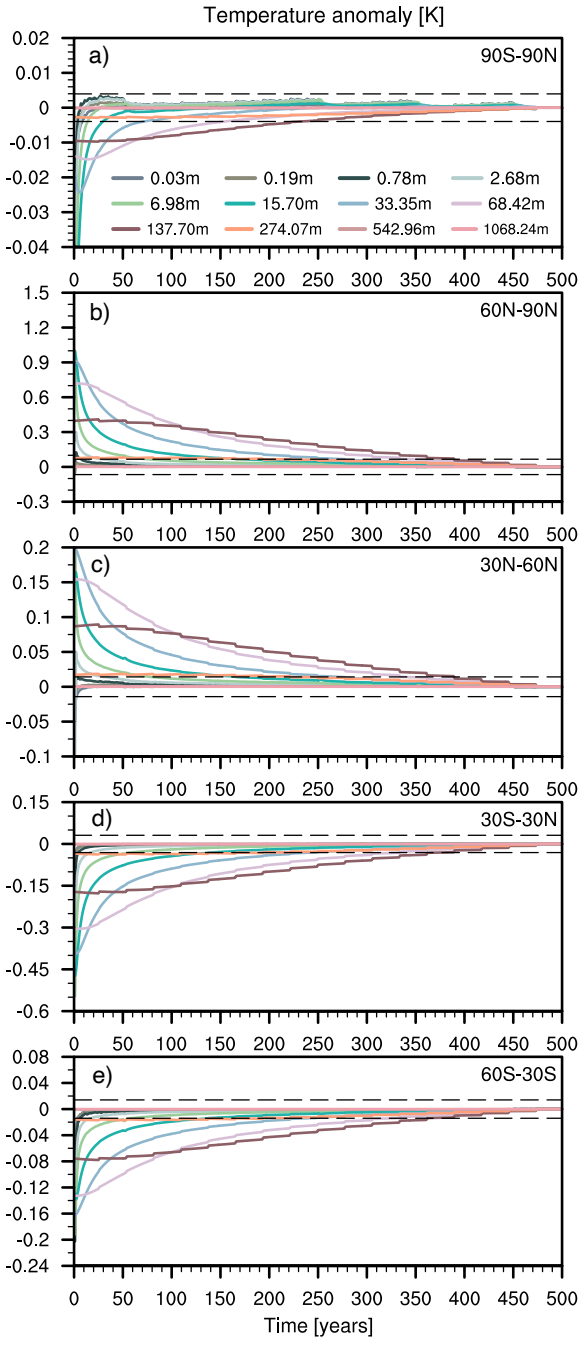

FIG. 5. Soil temperature anomalies [K] in the 12L PIC experiment with respect to the last 28 years (years 473 – 500 in the shaded time interval in Fig. 3) of the simulation for: (a) global (90°S–90°N); (b) Northern Hemisphere high latitudes (60°N–90°N); (c) Northern Hemisphere mid latitudes (30°N – 60°N); (d) low latitudes (30°S–30°N); and (e) Southern Hemisphere mid latitudes (60°S – 30°S). Dashed lines depict two standard deviations from the mean for the resulting anomalies in the 500 years of simulation. Note the differences in the temperature y-axis scales.

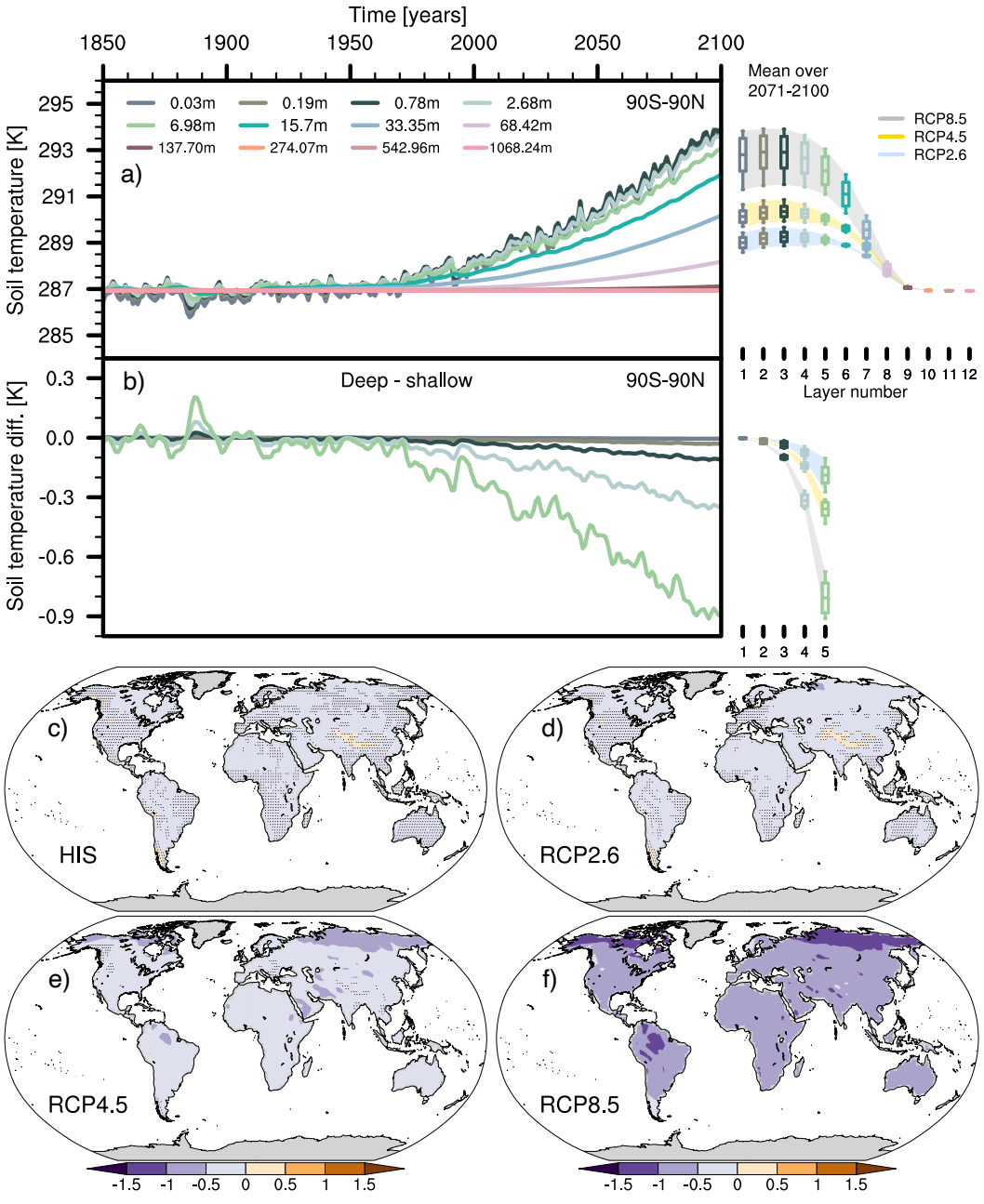

1059 FIG. 6. (a) Global absolute soil temperatures [K] in the 12L LSM configuration and (b) differences between
1060 the 12 and 5L configurations for the top 5 LSM layers in the historical and RCP8.5 simulations. Box and whisker
1061 plots indicate the range of temperature variability (a) and differences (b) for each soil layer and in the three RCP
1062 scenarios during the last 30 years of simulation. Box length stands for a range of two standard deviations, with
1063 the mean mark inside and the whiskers showing the levels for the minimum and the maximum. (c – f) Soil
1064 temperature differences (K) between the deep 12L and the shallow 5L configuration at the fith layer (9.83 m) of
1065 the last 30 years of the historical (HIS) simulation, the RCP2.6, RCP4.5 and RCP8.5 simulations. Points without
1066 stippling show significant differences (Student's t-test, $p < 0.05$).

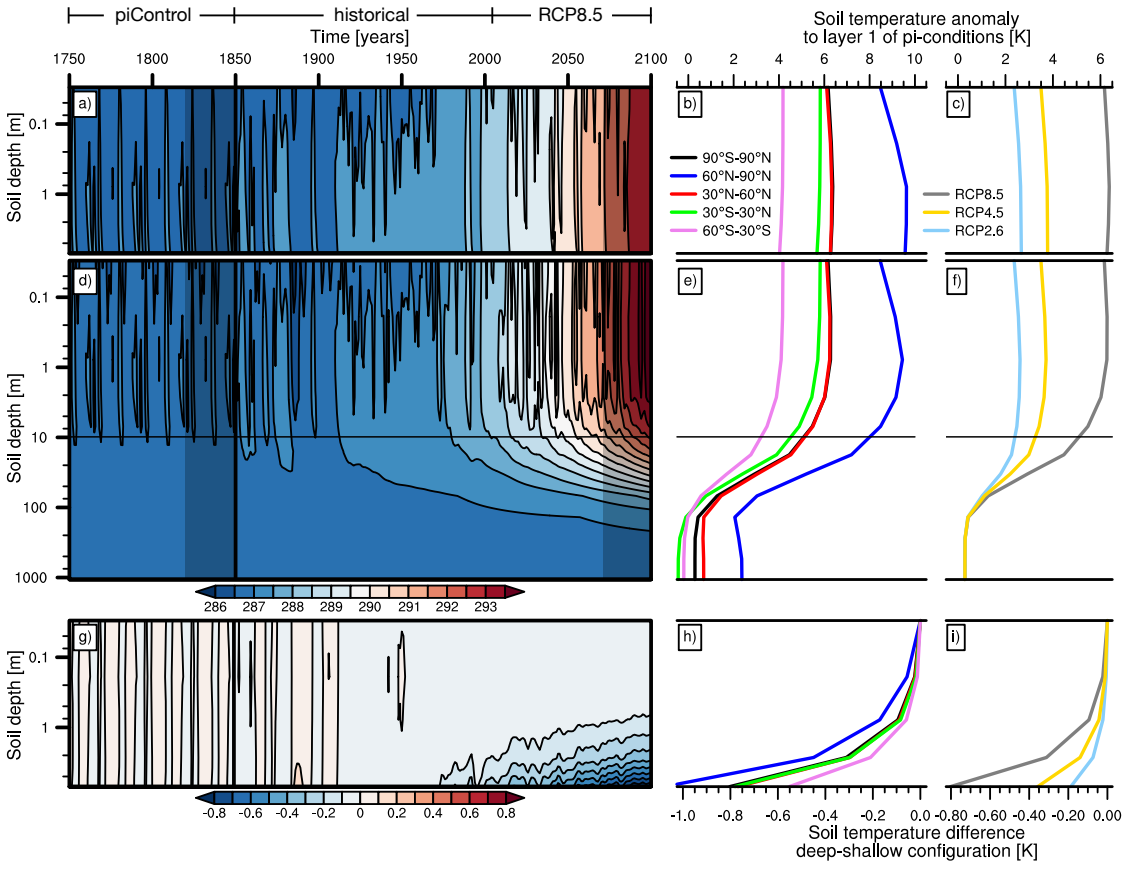

FIG. 7. (a) Hovmöller diagram of the absolute global temperature [K] *vs.* depth [m] for the last 100 years in the piControl simulation (dates are arbitrary and do not correspond to actual dates in forcing in PIC) continued into the historical (1850 – 2005) and RCP8.5 (2006 – 2100) simulations for the 5L configuration (d) the 12L configuration (g) soil temperature differences [K] for the first 5 layers in between the deep 12L and the shallow 5L configurations. (c) Soil temperature anomaly profiles for the last 30 years in the RCPs scenario ($\bar{T}_{2071-2100}$; dark shaded area) relative to the temperatures of the first soil level at the end of the piControl simulation ($\bar{T}_{1825-1850}$; dark shaded area) for the shallow 5L (f) the deep 12L configuration and (i) the differences between them for the first 5 model layers. For the RCP8.5, profiles are shown specifically also for several latitudinal bands for the (b) shallow, (e) deep and (h) for the differences.

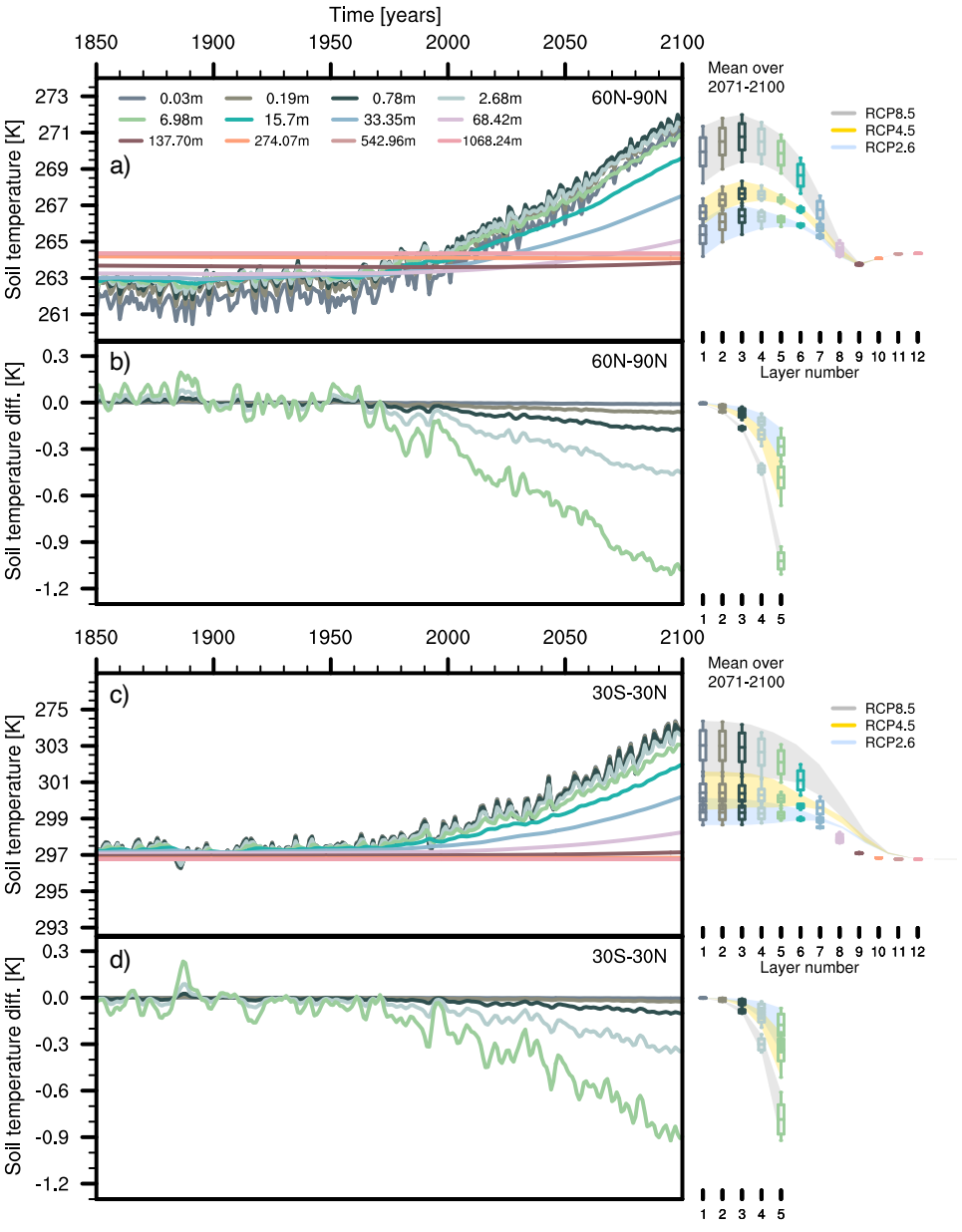

1076 FIG. 8. As Fig. 6 for different latitudinal bands (see legend): (a,b) NH high latitudes (60°N–90°N) and (c,d)
1077 intertropical regions (30°S–30°N). Note that, while the vertical scale is different for each latitudinal band, the
1078 temperature range is the same for each panel in order to make them comparable.

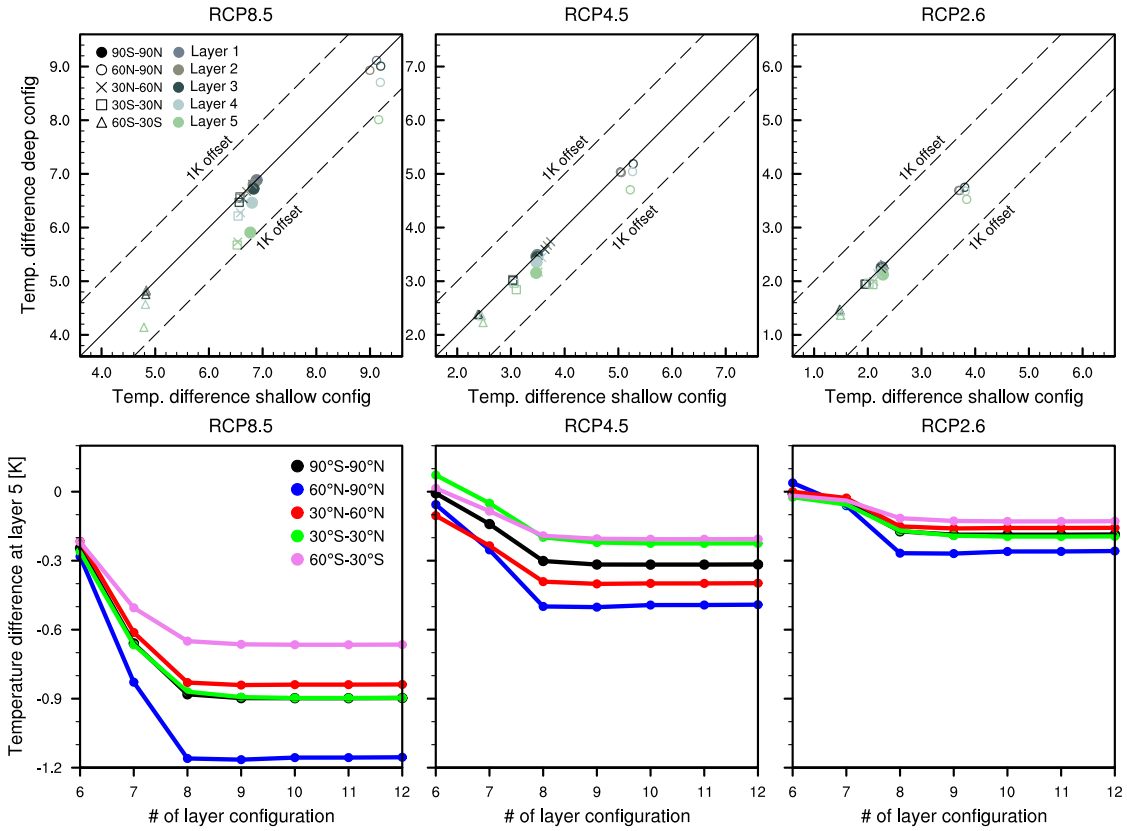

1079 FIG. 9. (Top row) Subsurface temperature differences [K] between the end of the 21st century and the pre-
1080 industrial temperature ($\bar{T}_{2095-2100} - \bar{T}_{1850-1855}$) for the 5-layer shallow (x-axes) and 12-layer deep (y-axis) soil
1081 model configuration for various layers (colors) and latitudinal bands (symbols). Note that the y-axis temperatures
1082 cover different ranges. (Bottom row) Soil temperature differences [K] at layer 5 between LSMs with a given
1083 number of layers (x-axis) that progressively increase from 6 to 12 and the reference 5L configuration. Colors
1084 stand for the various latitudinal bands.

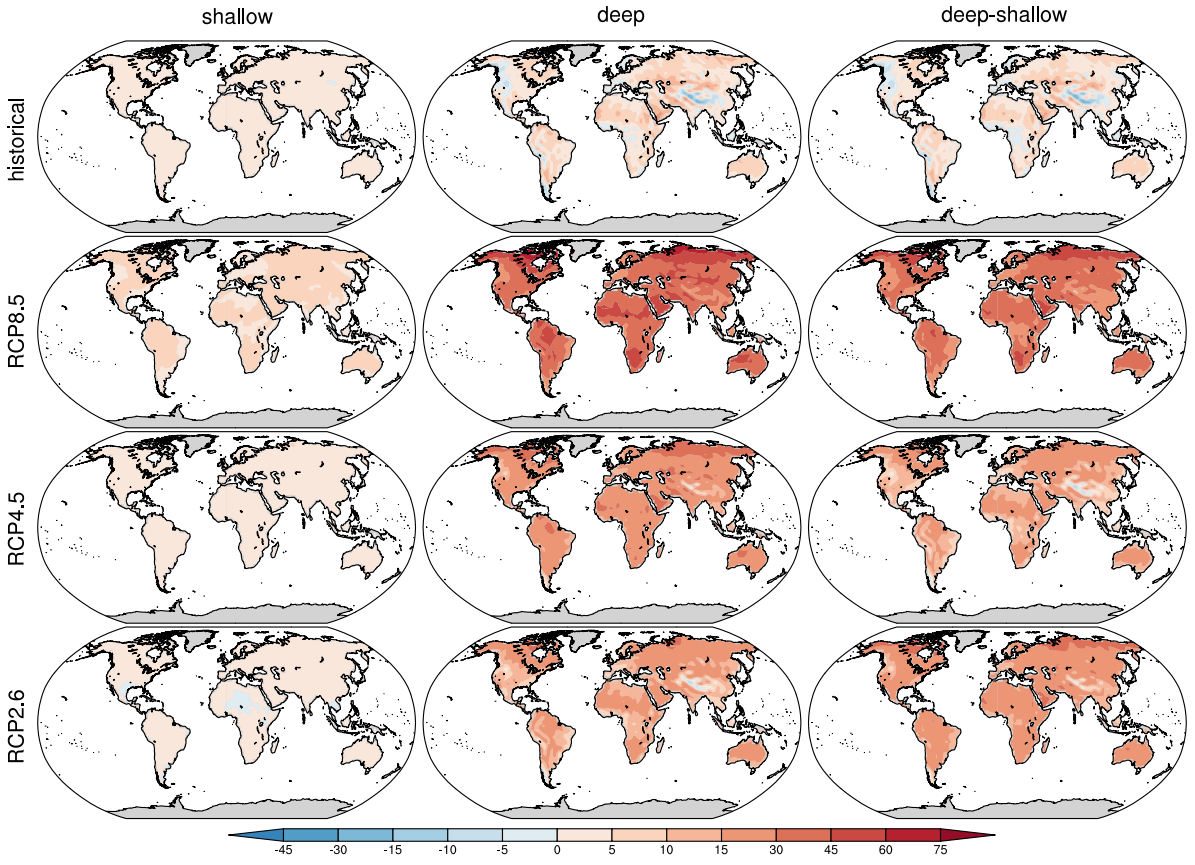

FIG. 10. (Left column) Annual heat content change $[10^5 Jm^{-2}yr^{-1}]$ relative to piControl in the shallow 5L and (Middle column) deep 12L LSM configurations for the historical (1850 – 2005), the RCP2.6, RCP4.5 and RCP8.5 (2006 – 2100) simulations (row 1 to 4). (Right column) Annual heat content change $[10^5 Jm^{-2}yr^{-1}]$ differences between the deep 12L and shallow 5L LSM configurations for each case. Polar ice sheets are not included.

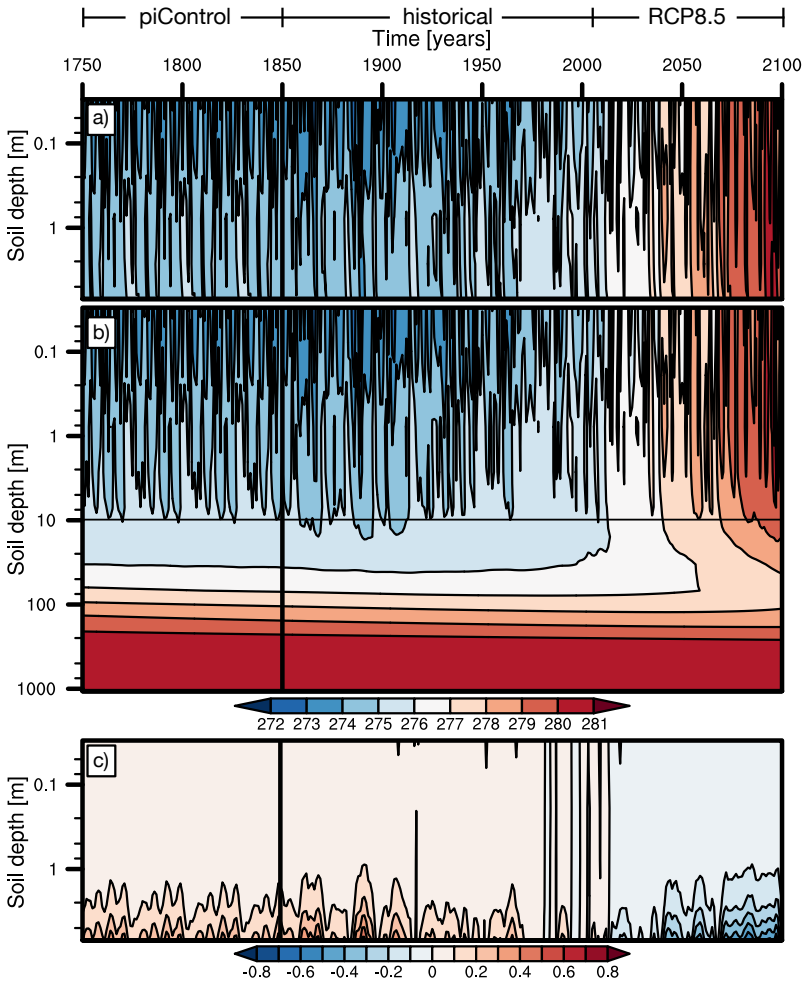

1090 FIG. 11. (a) Hovmöller diagram of the absolute temperatures [K] *vs.* depth [m] at a gridpoint in western US
1091 (45.7° N, 112.5° W) for the last 100 years in the piControl simulation (dates are arbitrary and do not correspond to
1092 actual dates in forcing in PIC) continued into the historical (1850 – 2005) and RCP8.5 (2006 – 2100) simulations
1093 for the 5L configuration, (c) the 12L configuration and (c) soil temperature differences (K) for the first 5 layers
1094 in between the deep 12L and the shallow 5L configurations.

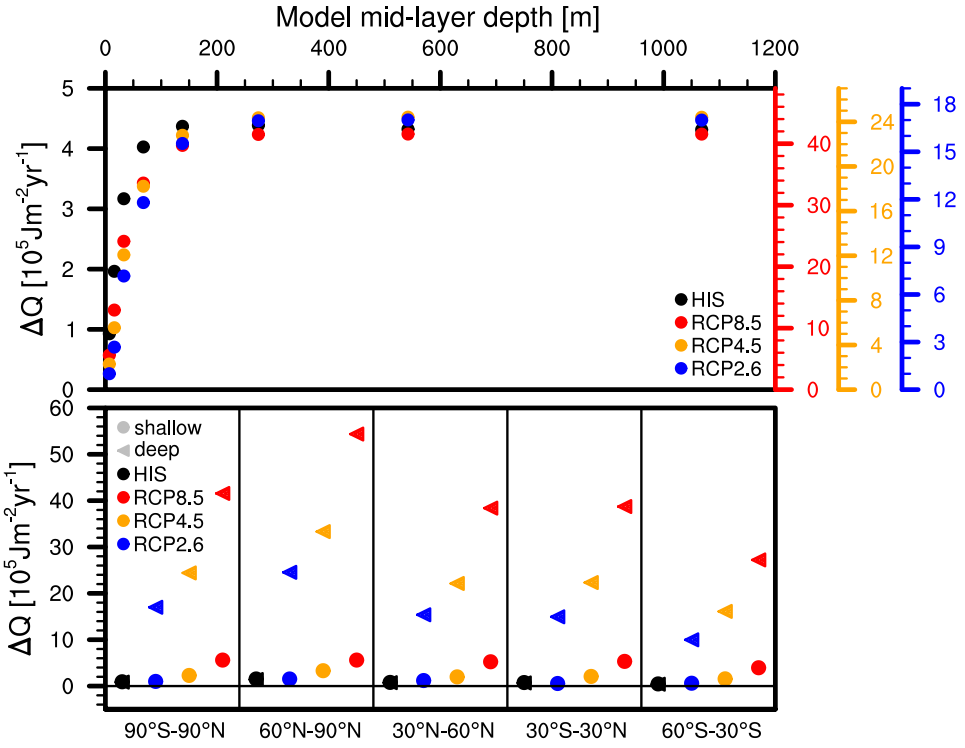

FIG. 12. (Top) Global mean annual heat content change $[10^5 Jm^{-2}yr^{-1}]$ in dependence to BBCP-depth configuration for HIS (left axis) and the RCP simulations (right axis). Results are shown for stepwise increases from the 5L to the 12L configuration. (Bottom) Area mean annual heat content change $[10^5 Jm^{-2}yr^{-1}]$ in the shallow (circles) and deep (triangles) LSM configurations, for global, NH high latitudes, NH mid latitudes, intertropical regions, SH mid latitudes and SH high latitudes.